CHALMERS
UNIVERSITY OF TECHNOLOGY

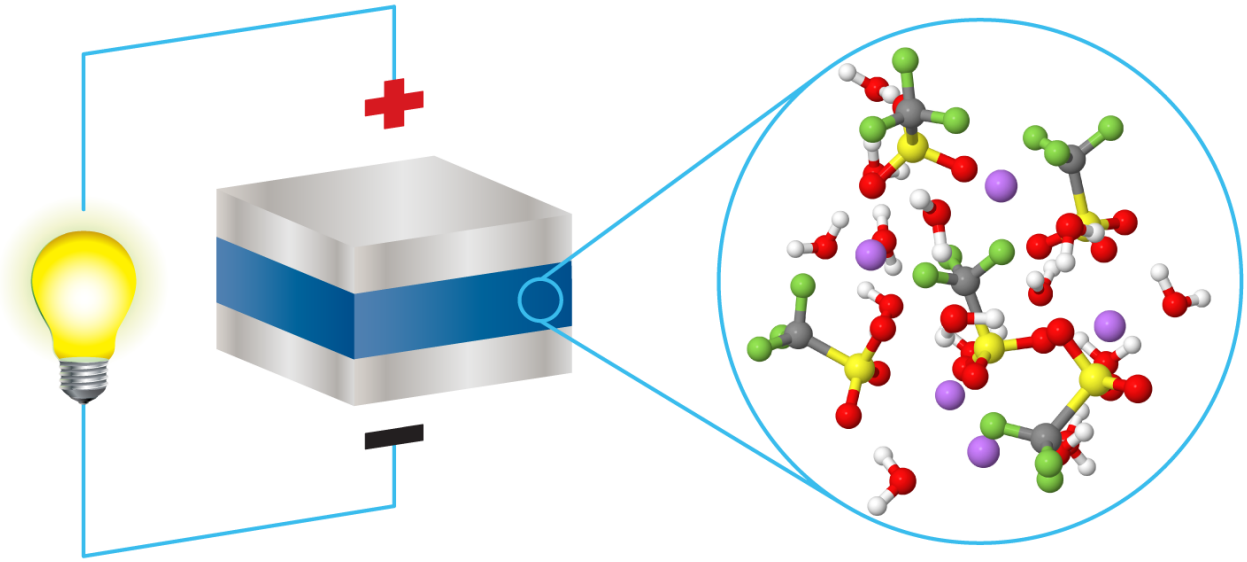

Aqueous Electrolytes for Next Generation Batteries

A study on highly concentrated water-based electrolytes

Master's thesis in Applied Physics

ALICE HAMRIN
ELLEN SCOTT

Department of Physics
CHALMERS UNIVERSITY OF TECHNOLOGY
Gothenburg, Sweden 2018

Master's thesis 2018

Aqueous Electrolytes for Next Generation Batteries

A study on highly concentrated water-based electrolytes

ALICE HAMRIN
ELLEN SCOTT

CHALMERS
UNIVERSITY OF TECHNOLOGY

Department of Physics
Division of Condensed Matter Physics
Chalmers University of Technology
Gothenburg, Sweden 2018

Aqueous Electrolytes for Next Generation Batteries
A study on highly concentrated water-based electrolytes

ALICE HAMRIN
ELLEN SCOTT

Examiner: Patrik Johansson, Department of Physics
Supervisors: Patrik Johansson, Adriana Navarro Suárez, Gustav Åvall, Department of Physics

Master's Thesis 2018
Department of Physics
Division of Condensed Matter Physics
Chalmers University of Technology
SE-412 96 Gothenburg
Telephone +46 31 772 1000

Cover: Illustration of an aqueous electrolyte battery, by Adriana Navarro Suárez.

Typeset in LaTeX
Gothenburg, Sweden 2018

Aqueous Electrolytes for Next Generation Batteries
A study on highly concentrated water-based electrolytes
ALICE HAMRIN
ELLEN SCOTT
Department of Physics
Chalmers University of Technology

Abstract

In today's society the demand for green energy is increasing, which in turn increases the demand for batteries to store the energy with. Facing a large expansion in battery production, the demands on batteries being safe, environmentally friendly and economical with natural resources are raised. This thesis aims to investigate the possibility of using water-based electrolytes in batteries, to mitigate safety problems usually associated with solvents for electrolytes. The thesis digs deeper into the area of highly concentrated aqueous electrolytes and investigates which properties in the salts are responsible for the expanded voltage window seen in previous research on the subject. The study comprises a range of combinations in anions and cations chosen by cost, abundance and previous results. The anions chosen were triflate (Tf), thiocyanate (SCN^-) and bis(trifluoromethane)sulfonimide (TFSI) and the cations were lithium (Li^+), sodium (Na^+) and magnesium (Mg^{2+}).

Three main properties were in focus; the ionic conductivity, the solvation structure and the electrochemical stability window (ESW). The properties were examined experimentally with Raman spectroscopy, dielectric broadband spectroscopy and linear sweep voltammetry, and computationally with semi-empirical and density functional theory (DFT) calculations. The study found LiTf to have the largest ESW at 3.25 V. The majority of the investigated systems show potential for solid-electrolyte interphase (SEI) formation for highly concentrated aqueous electrolytes, and an expanded ESW, possibly as a result of this SEI formation.

Keywords: Aqueous electrolytes, Highly concentrated electrolytes, Electrochemical stability window, Next Generation Batteries, PM7

Acknowledgements

First we would like to thank our supervisors Adriana Navarro Suárez and Gustav Åvall for supporting us and helping us throughout the project. We would also like to thank our supervisor Patrik Johansson for giving us the opportunity to be a part of the KMF group and broaden our knowledge about aqueous electrolytes. We would like to give our warmest thanks to all the people at the KMF division for immediately making us feel part of the gruop. This thesis project would not by far have been as much fun without you. Last but not least we would like to thank James Stewart, a.k.a Mr. MOPAC, for his support that allowed us to move forward with our project.

Alice Hamrin and Ellen Scott, Gothenburg, June 2018

Contents

List of Figures

List of Tables

List of Abbreviations

Molecules

TFSI	Bis(trifluoromethanesulfonyl)imide	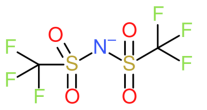
Tf	Trifluoromethanesulfonate	
SCN^-	Thiocyanate	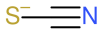

Abbreviations

ESW	Electrochemical stability window
WiSE	Water-in-salt electrolyte
SiWE	Salt-in-water electrolyte
SEI	Solid-electrolyte interphase
SSIP	Solvent separated ion pairs
CIP	Contact ion pairs
AGG	Ionic aggregates
HOMO	Highest occupied molecular orbital
LUMO	Lowest unoccupied molecular orbital
DFT	Density functional theory
HF	Hartree-Fock
PM7	Parametric model 7
DOS	Density of states
IR	Infrared
LSV	Linear sweep voltammetry
PES	Potential energy surface
RDF	Radial distribution function
m	Molal
LIB	Lithium-ion battery
FTIR-spectroscopy	Fourier transform infrared spectroscopy

1
Introduction

By 2040 the global energy demand is expected to grow by almost 30 % [1]. With the energy production of today we are predicted to cause an increment in the global temperature of more than 3°C only during the 21st Century [2] causing irreversible damage to our environment. The growing energy consumption and increasing threat to our climate calls for a great change in how we produce and consume energy. The approaching climate change has also led to concrete action in terms of the Paris Agreement [3] where 175 countries agreed on limiting the global warming to below 2°C in 2016.

A large portion of the energy we use today is produced from burning fossil fuels. One of the most immediate issues with this energy recovery method is the high amount of carbon dioxide it releases into the atmosphere [4, 5]. Alternative renewable energy sources often have a hard time competing with the mobility and accessibility of fossil fuels. Energy production from solar cells, wind power or wave power all have the disadvantages of being unreliable in terms of when they produce energy and with no direct possibility of storing the energy for later use. Batteries are therefore a crucial component in the upcoming sustainable energy system and are the focus of many research investments around the world.

The rapid development of the lithium-ion batteries (LIBs) in terms of energy density, *i.e* the amount of energy stored per unit mass or unit volume of the battery, in the last decades has put them on the map as the leading battery technology. However, facing a transition towards sustainable transportation systems all over the world the battery industry will have additional aspects to consider as the demand for batteries increases. Large scale production of batteries puts higher demands on abundance of materials, environmental sustainability and safety.

Even though LIBs are a widely used type of battery, concerns related to their safety, cost and environmental friendliness have been raised [6]. Batteries rely on ion transport as charging and discharging mechanism. The electrolyte enables transport of charge carriers between anode and cathode but does not allow electric current to flow. The most commonly used electrolytes are based on the lithium heaxaflourophosphate ($LiPF_6$) salt together with ether-based solvents, and these are highly flammable and reactive with the charged electrodes and $LiPF_6$ is thermally unstable and toxic. Aqueous electrolytes could be a solution to these safety, cost and environmental concerns. However, their electrochemical stability window is too narrow leading to a low energy density which make them incapable of large

scale applications. Recently, research has been done on highly concentrated aqueous electrolytes with the hope of achieving an expanded ESW with high enough salt concentrations. These highly concentrated water-in-salt electrolytes (WiSE) systems have proved to possess unique properties compared to the more diluted salt-in-water (SiWE)[6, 7].

1.1 Aim of the project

This master thesis project investigates the usage of aqueous electrolytes in batteries, aiming to improve the safety issues and environmental impacts associated with non-aqueous electrolytes. This thesis project will investigate a broader variety of battery chemistries for WiSE than studied before. Earlier studies in the subject have led to the observation that when the electrolyte goes from being a SiWE to a WiSE most of the ions are in aggregated form which has a correlation with formation of a solid electrolyte interphase (SEI) and an increased stability against redox reactions[7]. The electrochemical stability of the electrolyte against reduction and oxidation can be measured in terms of the ESW. The study aims to confirm the results from earlier studies on lithium bis(trifluoromethane)sulfonimide (LiTFSI) and sodium triflate (NaTf) and to confirm this behaviour in battery chemistries where this correlation has not yet been investigated. The battery chemistries under examination are those with the charge carrying cations lithium (Li^+), sodium (Na^+) and magnesium (Mg^{2+}) and the anions TFSI, Tf and thiocyanate (SCN^-). Along this study, the following questions will be answered:

- Which of the chosen battery chemistries show potential for an expanded ESW of aqueous electrolytes?
- How does divalent cations affect the conductivity and solubility?
- What battery chemistry is best suited for applying WiSE?
- Can any other battery chemistry be predicted to have potential to use WiSE based on the results of this study?

2

Background and Theory

2.1 Batteries

A battery is a device that converts chemical energy to electrical energy through reduction and oxidation (redox) reactions. It consists of several electrochemical cells each consisting of two electrodes, an electrolyte and a separator preventing the electrodes from short circuiting. When the battery is discharging, electrons flow from the negative electrode, *i.e.* the anode, through an external circuit to the positive electrode, the cathode. Meanwhile, ions flow through the electrolyte from the anode to the cathode. In order to enable this the electrolyte must be electron insulating and ion conducting. A schematic of the working principle of an electrochemical cell during discharge is shown in figure 2.1.

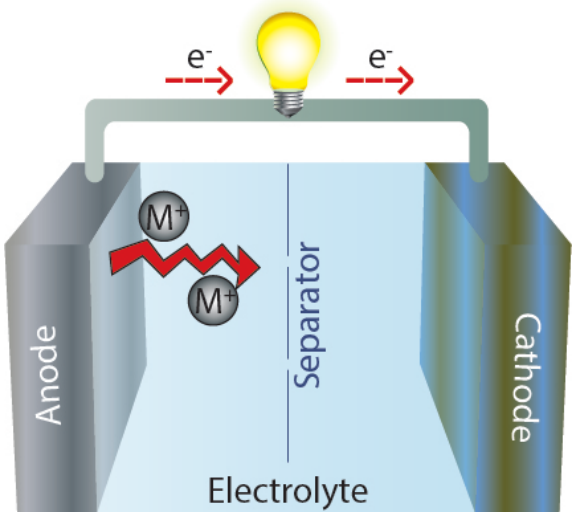

Figure 2.1: Working principle of an electrochemical cell during discharge. Cations move from the anode to the cathode through the electrolyte and electrons are being transferred through an external circuit.

There are two categories of batteries, primary and secondary batteries. Primary batteries are used once and then disposed while secondary batteries can be recharged and used several times. In 1800, Volta first described the battery through his voltaic pile [8] consisting of alternating disks of zinc and silver with a cloth soaked in electrolyte placed in between the metals. Volta got his voltaic pile idea from Galvani who claimed to have discovered "animal electricity". Galvani realized that when

touching a frog with two metal objects the muscles in the frog contracted and he believed that these electric pulses were generated within the muscles. However, Volta was skeptic about this and instead he concluded that the blood acted as an electrolyte between the two metals creating an electric current through the body. Hence, the battery was invented. The first widely used primary battery was the Leclanché cell consisting of a zinc anode, a manganese dioxide cathode and an acidic aqueous electrolyte. It was invented by the french engineer Georges Leclanché in 1865 [8]. Today, commonly used alkaline batteries are examples of primary batteries using the same anode and cathode but with an alkaline electrolyte.

The charging process in the secondary batteries is made possible by supplying external electric energy which is converted into chemical energy and stored in the battery. During charging the electrons and ions flow in the opposite direction compared to the discharge process.The first rechargeable battery was the lead acid battery which was invented by the french physicist Gaston Planté in 1859. It is still the most used battery in the world, mostly used for ignition batteries in cars and stands for 70 % of the total amount of rechargeable batteries sold [9]. Although this early rechargeable battery technology is still used, the LIB is the most widely researched technology today. The technology was first commercialized in 1991 by Sony Corporation [10] and is today used in portable electronics such as mobile phones and laptops. The battery possesses great advantages such as high energy density, high output voltage, high power and fast charge and discharge. Lithium is a very light material and this in combination with a small radius provides the high energy density. However, lithium is a limited resource with only 20 ppm abundance in the Earth's crust [11]. Alongside this, cobalt, which is used in the electrode material, is mined in the Democratic Republic of Congo, a region of conflict. Due to this, new battery technologies for next generation batteries are researched with a reduced or no amount of lithium.

2.2 Non-aqueous electrolytes

Commercial LIBs uses non-aqueous electrolytes, most common is the $LiPF_6$ salt solvated in organic carbonate solvents, such as ethylene carbonate, propylene carbonate, dimethyl carbonate, ethyl methyl carbonate and diethyl carbonate [12]. The solvents are either pure or mixtures of different ratios together with additives. Using non-aqueous electrolytes, an SEI is formed kinetically stabilizing the electrolyte [13]. The electrolyte components decompose irreversibly producing solid products which then deposit on the electrode surfaces forming the SEI. This is due to operation at a potential beyond the electrolyte's thermodynamical stability limit in order to improve the energy output. When the interphase has formed, it prevents further decomposition of the electrolyte while allowing for the electrochemical reactions to continue. The SEI acts as an insulator towards electrons and a conductor towards ions and it significantly expands the ESW.

The formation of an SEI is crucial for the performance of the battery [14], however, these organic electrolytes are flammable and volatile which makes them unsafe.

2.3 Aqueous electrolytes

Water is considered to be the universal solvent since it has the capability of dissolving a large range of different compounds. This is due to the polarity of the water molecule; being negatively charged at the oxygen site and positively charged at the hydrogen site. In the case of dissolving salt, water is thus able to dissolve both the positively charged cations and the negatively charged anions. This makes water an interesting solvent to use for electrolytes. However, in conventional aqueous electrolytes, opposed to non-aqueous electrolytes, an SEI does not form given that the decomposed components of the electrolyte solvent (water), H_2, O_2, OH^-, can not deposit in solid state on the electrodes. This limits aqueous-based batteries to narrow voltage windows. However, recent results [6] has shown that at sufficiently high salt concentrations of TFSI and Tf, for WiSEs an interphase is formed by degradation products of anions.

In addition to its ability to form a SEI, the WiSEs have also shown potential for an expanded ESW compared to the conventional, more diluted, SiWEs. This is another desirable property, bringing the aqueous electrolytes closer to being a competitive option for commercial batteries. This aqueous option for electrolyte can contribute to the safety and environmental aspects as mentioned above, however the LiTFSI salt is expensive [15] due to a complex synthesis and considering the high amount of salt required. Thus finding a cheaper salt with similar properties is necessary in order to make this technology commercially available.

2.3.1 Solvation structure and SEI formation

When using aqueous electrolytes, high salt concentrations are required in order for the formation of an SEI to occur. Depending on the system, concentrations above 20 m (molal, moles solute/kg solvent) could be necessary [6]. At such a high concentration, the anions are mainly contained within the primary solvation shell of the cation. At more diluted concentrations the anions and cations are coordinated as solvent separated ion pairs, SSIPs, where the anion is contained within the second solvation shell of the cation, whilst the solvent molecules (water) are located within the primary shell, see figure 2.2. As the concentration increases the anion enters into the primary solvation shell of the cation and forms contact ion pairs, CIPs, and ionic aggregates, AGGs, where the cation is surrounded by more than one anion [16]. Hence, the amount of CIPs and AGGs increases with concentration.

With increased salt concentration there is a high probability of an anion being confined within the cation primary solvation shell. During these conditions, in the case of TFSI and Tf anion systems, the reduction of the anion becomes dominant due to the shift of both the anion conduction band minimum and the water valence band maximum to lower potentials. The reduction of the anion leads to a sufficient amount of metal-fluorine formation, making up the protective SEI.

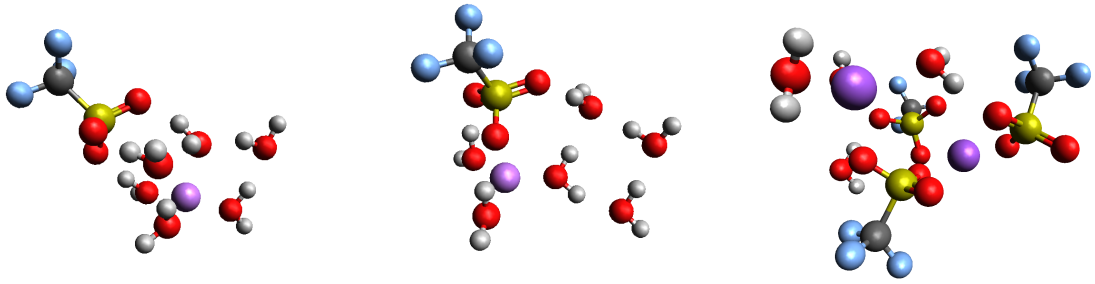

(a) SSIP (b) CIP (c) AGG

Figure 2.2: Illustrations of example geometries representing LiTf in (a) solvent separated ion pairs (SSIP), (b) contact ion pairs (CIP) and (c) aggregated ion pairs (AGG).

2.4 Quantum mechanical calculations

In order to make an estimate of the ESW of the electrolytes under investigation, the reduction and oxidation potentials of ions and water molecules should be calculated at several concentrations. The redox potentials can be calculated with quantum mechanical (QM) computational methods. Two main approaches for determining redox potentials can be found in literature [17]; the thermodynamic cycle approach, using the Gibb's free energy of the reaction chain to determine the Gibb's free energy of reduction/oxidation in solvent phase, and the linear free energy relationship method (LFER) where the potentials are assumed to depend linearly on electronic properties like for example HOMO/LUMO energy levels [17].

2.4.1 Semi-empirical methods

Predicting ground state properties of molecular systems is something scientists have striven for since quantum mechanics first was introduced. Solving the full Schrödinger equation is possible for single electron systems but become unfeasible for larger systems. The complexity in the interactions in many-body systems forces us to use approximations to describe correlation and exchange effects in methods such as the Hartree-Fock (HF) model. In the HF model the main approximations are the central field approximation and the use of a guessed functional form of the wavefunction [18]. Since the HF model is of variational form, the energies calculated with this approximation will always be greater than the actual values.

Semi-empirical methods are quantum mechanical methods based on the Hartree-Fock formalism. The semi-empirical methods can consider some electronic correlation effects, however, there are some major simplifications made to the HF model. Often the two-electron integrals are approximated or omitted and some parameters are obtained from fittings to experimental data. The simplified and empirical nature of the methods allow them to solve larger molecular systems at lower computational

cost and can handle energy calculations of systems of up to 10000 atoms.

2.4.2 Density functional theory

Although accurate for small systems, the HF model do come at a high computational cost as the number of electrons in the system increases. A simpler and more cost efficient way of calculating electronic properties can be found in the density functional theory (DFT). Already in the 1920's Thomas and Fermi suggested that statistical theory can be used to describe the electronic distribution of the atoms[19, 20]. The theory also gave rise to the local density approximation (LDA) which assumes that electronic properties are locally dependent on the electron density ($\rho(r)$). This was later confirmed when Hohenberg and Kohn published their paper in the 1960's presenting the theorems behind a theory called density functional theory [21]. The theory introduces a density functional and proves that it has a variational principle, showing that there exists a ground state density for which this density functional is minimized. Now the ground state energy can be given by the minimum of the energy functional

$$E[\rho] = \int \rho(\mathbf{r})v(\mathbf{r})d\mathbf{r} + F(\rho) \tag{2.1}$$

where $F[\rho] = T[\rho]+V_{ee}[\rho]$; the sum of the kinetic energy functional and the electron-electron interaction potential [18]. Still, the theory was not very useful until Kohn and Sham presented a method for solving the equations in an efficient way. In this method the interacting molecules are replaced with fictitious non-interacting molecules, making it possible to solve this fictitious system exactly, and in this way obtain a better approximation for the electron density. The energy functional was rewritten on the form

$$E[\rho] = T'[\rho] + \int [\hat{V}_{ext}(r) - \hat{U}_{el}(r)]\rho(r)dr + E_{xc}[\rho] \tag{2.2}$$

where now, $T'[\rho]$ is the kinetic energy of a fictitious system with the same electron density as the system we seek electron density of, but with non-interacting electrons [18]. $\hat{U}_{el}(r)$ is the Coulomb interaction between electrons, $\hat{V}_{ext}(r)$ is the external potential, *i.e.* the potential from the nuclei, and $E_{xc}[\rho]$ is the exchange-correlation functional which includes all terms missing from the other terms; electron exchange, electron correlation, corrections for the fictitious kinetic energy, $T'[\rho]$, not being identical to the actual kinetic energy of the system, $T[\rho]$, and self correlation. All computationally difficult parts are now put into the exchange-correlation functional which is approximated using different functionals to describe the electron density and other electronic properties as accurately as possible.

In this study the Minnesota-06 exchange-correlation functional, M06-2X, is used. This is an approximation for the exchange-correlation functional based on constraints satisfaction, empirical fits and mixing DFT and HF exchange [22]. The M06-2X is highly non local and has double the portion of non local exchange compared to the M06 functional.

2.4.3 Density of states

The density of states (DOS) can tell us a lot about the structure and electronic behaviour of a material. The DOS is defined as the number of states of a system per unit volume and energy or per d$\mathbf{k}^3$ in k-space [23]. To demonstrate the DOS in a simple case we derive the density of state for a particle in a box. Each state is separated by $\frac{\pi}{L_x}$ in k-space, implying that every state takes up a volume of $\frac{\pi^3}{L_x L_y L_z}$ in reciprocal space, where L_i are the lengths of the box's sides. The state density is then $\frac{L_x L_y L_z}{\pi^3} = \frac{V}{\pi^3}$. The number of states N within a spherical volume with radius k is the volume of the shell times the state density with a multiplicity of 2 for the two spin states

$$N = \frac{4\pi k^3/3}{\pi^3/V} \cdot \frac{2}{8} = \frac{Vk^3}{3\pi^2} \tag{2.3}$$

To avoid counting wavefunctions with different signs twice the expression is also divided by 2^3 to count only positive n_x, n_y, n_z states. Using the relations $p = \hbar k$ and $E = p^2/2m^*$ implying $E = \hbar^2 k^2/2m^*$, where m^* is the effective mass of the carriers and E is the energy relative to the conduction band onset, we get the expression

$$k^2 = \frac{2m^* E}{\hbar^2} \tag{2.4}$$

inserting (2.4) in (2.3) gives

$$N = \frac{V(\frac{2m^* E}{\hbar^2})^{3/2}}{3\pi^2} = \frac{V}{\pi^2}\left(\frac{2m^* E}{3\hbar^2}\right)^{3/2} \tag{2.5}$$

Finally, the DOS can be obtained as the derivative of the number of states with respect to the energy[24].

$$D(E) = \frac{\partial N}{\partial E} = \frac{\partial}{\partial E}\left[\frac{V}{\pi^2}\left(\frac{2m^* E}{3\hbar^2}\right)^{3/2}\right] = \frac{V}{2\pi^2}\left(\frac{2m^*}{\hbar^2}\right)^{3/2}\sqrt{E} \tag{2.6}$$

We then obtain the relation $D(E) \propto \sqrt{E}$, however, this relation is only valid for the particle in a box system. More importantly the DOS can reveal the highest occupied molecular orbital (HOMO) and lowest unoccupied molecular orbital (LUMO) energies of a system since the onsets for the nonzero parts of the DOS will be situated at the HOMO/LUMO energies. The HOMO/LUMO energies can then be used to estimate the ESW.

2.5 Infrared spectroscopy

Vibrational spectroscopy, in this study IR and Raman spectroscopy specifically, is a technique used to characterize molecular structures and will here be used to investigate the coordination between anions and cations in the electrolytes. Infrared (IR) spectroscopy relies on the absorption of IR light by a molecule which is determined by the vibrations of the molecule [25]. Upon absorption of IR radiation the transition between molecular vibrational energy levels is measured. In order

for a molecule to be IR-active it must have a dipole moment which changes during vibration. The dipole moment μ of a molecule is given by

$$\mu = \sum_i e_i r_i \tag{2.7}$$

where e_i is the magnitude of the atomic charges and r_i is the position of the atom. The change in the dipole moment allows for the molecule to absorb the energy from the radiation which leads to a change in the vibrational energy level. This can be compared to the Raman spectroscopy where the molecular vibrations must cause a change in the polarizability in order for the molecule to be Raman-active.

In IR spectroscopy frequencies from different ranges can be emitted, the near-IR ranged from 14000-4000 cm^{-1}, mid-IR ranges from 4000-400 cm^{-1} and the far IR ranges from 400-10 cm^{-1}. Normally the mid IR range is used. The results from the IR-measurement are presented as a plot of the intensity, which can be either absorbance or transmittance, against the wavenumber.

2.6 Raman spectroscopy

In contrast to infrared spectroscopy which takes advantage of the absorbance of light in a material the Raman spectroscopy relies on inelastic scattering of light [26]. When light interacts with a material the oscillatory nature of the incident electric field together with oscillations in the susceptibility causes sidebands which correspond to light frequencies shifted by the phonon frequencies. These sidebands are usually referred to as Raman-scattered light waves and their frequency shifts due to the phonon interaction are the Stokes and anti-Stokes shifts, for positive and negative shifts by the phonon frequency ω_p respectively [27].

In a quantum physical interpretation of the phenomenon, the process can be described in 3 steps; the generation of a electron-hole pair by a photon, creation or annihilation of a phonon and the recombination of the electron-hole pair giving rise to radiation of a photon. The scattering is illustrated in figure 2.3. Here the coupling between the processes is what determines the intensity of the Raman scattered light. The Stokes or anti-Stokes shifts represent exciting or depleting the molecule between vibrational levels and the ground state. Since the ground state is more populated than the excited vibrational states, the Stokes shift will always show a higher intensity than the anti-Stokes shift [26]. A classic Raman spectroscope uses a monochrome excitation laser, gratings and a detector with low background level.

2.7 Dielectric broadband spectroscopy

Dielectric broadband spectroscopy is a technique which falls under the category of impedance spectroscopy and can be used to measure the conductivity of a sample.

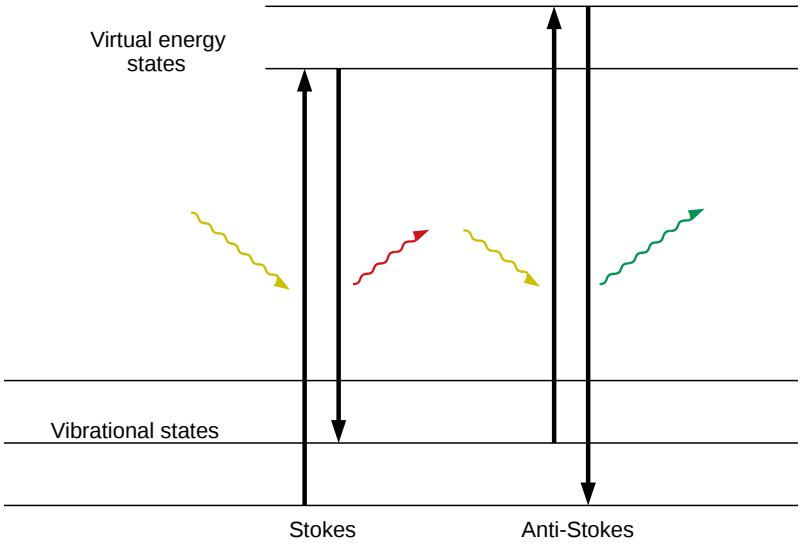

Figure 2.3: Illustration of Raman scattering.

In dielectric spectroscopy, the response field of a sample is observed after applying a disturbance to it [28]. In this case the disturbance is a time dependent external electric field and the response field observed is the polarization field of the sample. When applying small external fields $E(t)$ the response can be considered linear, which yields the expression for the polarization response

$$P(t) = \chi\varepsilon_0 E(t) = \varepsilon_0(\varepsilon_r - 1)E(t) \tag{2.8}$$

where $P(t)$ is the polarization, χ is the susceptibility, ε_r the relative permittivity and ε_0 is the vacuum permittivity. The expression can also be used to rewrite the dielectric displacement vector $D(t) = \varepsilon_0 E(t) + P(t)$, yielding

$$D(t) = \varepsilon_0 \varepsilon E(t) \tag{2.9}$$

Now we introduce a harmonic external field $E(\omega) = E_0 e^{i\omega t}$, where E_0 is the amplitude of the external field and ω is the angular frequency, yielding a displacement field $D(\omega) = D_0 e^{i(\omega t + \phi(\omega))}$ with the amplitude D_0 and the phase shift $\phi(\omega)$. By rewriting equation (2.9) and considering harmonic $E(t)$ and $D(t)$ we obtain the expression for the frequency dependent complex dielectric function

$$\varepsilon^*(\omega) = \varepsilon'(\omega) - i\varepsilon''(\omega) = \frac{D(\omega)}{\varepsilon_0 E(\omega)} = \frac{D_0 e^{i(\omega t + \phi(\omega))}}{\varepsilon_0 E_0 e^{i\omega t}} = \frac{D_0 e^{-i\phi(\omega)}}{\varepsilon_0 E_0} \tag{2.10}$$

with ε' and ε'' being the real and complex parts respectively.

In this work, the frequency region of interest was 10^{-1}-10^{6} Hz in which the dielectric function is obtained by treating the sample as a capacitor and measuring its complex capacitance $C^*(\omega)$ which is correlated to the dielectric function as

$$\varepsilon(\omega) = \frac{C^*(\omega)}{C_0} \tag{2.11}$$

where C_0 is the empty cell capacitance. The dielectric function of a capacitor can be expressed in terms of the impedance, which is given by $Z^*(\omega) = \frac{U^*(\omega)}{I^*(\omega)}$ when a harmonic voltage is applied to the capacitor. The expression for the dielectric function is then

$$\varepsilon^*(\omega) = \varepsilon'(\omega) - i\varepsilon''(\omega) = \frac{1}{i\omega\varepsilon_0 Z^*(\omega) C_0} \tag{2.12}$$

The complex conductivity σ^* can be obtained from the dielectric function with the following expression.

$$\sigma^* = \sigma' - i\sigma'' = i\omega\varepsilon_0(\varepsilon^* - 1) \tag{2.13}$$

2.8 Linear sweep voltammetry

Linear sweep voltammetry is a commonly used electrochemical analysis method for examining the electrochemical stability window of electrolytes. The method is based on applying a linearly varying potential difference over electrodes on the specimen and measuring the current flowing as a function of time. This results in a relation between applied voltage and current flowing through the sample. In linear sweep voltammetry the direction of the sweep is chosen based on whether the reduction or oxidation process is of interest.

When the electrolyte is reduced at the electrode a current flows, the reduced molecule flows away from the electrode and a new molecule enters the vicinity of the electrode where it is reduced [29]. This gives rise to a mass diffusion. An increased voltage will give rise to an increased current and in turn also an increased mass diffusion towards the electrode until the maximum limit of mass transfer is reached. In a reversible reaction the peak current will be limited by this maximum mass transfer rate. Analogously there will be a similar phenomenon for the oxidation process at negative potentials.

3
Implementation

3.1 Computational implementations and analysis

3.1.1 Start configurations

The configurations of electrolytes in different chemistries and concentrations were generated randomly in order to cover as large part of the PES as possible and in that way avoid sampling local minima to a high extent. The systems were chosen to contain 5 cations and the anions were in a 1:1 relation to the cation except for in the magnesium salt based systems where there were two anions for each cation. The water ratio was chosen to be 1:3, 1:6, 1:16 and 1:55 to the cation to represent the molal concentrations presented in table 3.1 for the respective electrolytes.

The systems were randomly generated in GROMACS [30] with the function *insert-molecules* and giving the function a random integer, in this way the software places the molecule randomly somewhere in the solvation box where it does not overlap with another molecule. A solvent box was generated in GROMACS, then the anions were inserted first, followed by the cations and last the water molecules. After the configurations had been randomly generated, they were optimized in Avogadro [31, 32] with the universal force field, UFF, in order to avoid high energy configurations and check for errors in the systems.

Table 3.1: Electrolyte salt concentrations.

Salt	**C [mol/kg]**		
LiTFSI	**3.47**	**9.25**	**18.5**
NaTFSI	**3.47**	**9.25**	-
MgTFSI	**1**	**3.47**	-
LiTf	**3.47**	**9.25**	**18.5**
NaTf	**3.47**	**9.25**	-
MgTf	**1**	**3.47**	-
LiSCN	**3.47**	**9.25**	**18.5**
NaSCN	**3.47**	**9.25**	**18.5**

3.1.2 Geometry optimization

In order to obtain information about the electrolytes under investigation the systems have to be in a state that is plausible in reality. Therefore all configurations were

optimized to reach the lowest possible heat of formation. The optimizations were performed with the PM7 method in the softwares Gaussian 16 [33] and MOPAC [34].

Most optimizations were performed in MOPAC where the optimization was repeated until reaching a stable heat of formation and a gradient norm below 0.2 per atom in the system. Since MOPAC uses heat of formation as the minimization parameter one can be sure that the state is a true minima in the potential energy surface when the heat of formation is stable for a long time and the gradient norm is small.

The configurations based on salts with the anion SCN^- did not converge during geometry optimization in MOPAC, therefore these systems were instead optimized using the PM7 method in Gaussian. In Gaussian the optimization runs were repeated until convergence was reached according to Gaussian. In Gaussian the optimization also had to be confirmed to be a true minima by performing a frequency calculation, zero imaginary frequencies from this calculation would then imply that the geometry is in a true minima on the PES.

3.1.3 Density of states

The electronic orbital information obtained from geometry optimization in PM7 was used to calculate the density of states distributions for the systems in the software GaussSum for geometries optimized in Gaussian 16 and Gabedit for geometries optimized in MOPAC. The spectra were obtained by convoluting the orbital energies with gaussian curves of width 0.3 eV. For systems of interest, the DOS was also obtained at DFT level by performing a single point calculation with a full population analysis in Gaussian 16 with the M06-2X/6-311+G* functional and basis set. The DOS and projected DOS could then be obtained in GaussSum.

3.1.4 Radial distribution functions

The radial distribution function represents the average number of atoms at a specific radial distance interval with respect to a reference atom. By calculating radial distribution functions for different atom types of interest, structures of a system can be revealed. For a crystalline structure the radial distribution function will consist of discrete spikes at the distances between lattice positions. In a liquid the function will have a continuous character with peaks at short distances leading in to a smoothed out plateau at large distances. The first peak in the curve represents the first solvation shell of which the atomic composition and distance from the reference atom can give important information about the structure of the liquid.

The partial radial distribution functions for different atomic species can be obtained from the expression

$$g_\alpha(r) = \frac{dn_\alpha(r)}{4\pi\rho_\alpha dr} \tag{3.1}$$

where $dn_\alpha(r)$ is the number of atoms of species α located in a spherical shell of thickness dr at the distance r from the reference atom and ρ_α is the density of α

atoms in the solvent [35]. Also, the number of atoms within the first solvation shell, the first coordination number, can be calculated from the radial distribution with the following expression

$$n_\alpha = 4\pi \int_{r_0}^{r_1} g_\alpha(r)\rho_\alpha r^2 dr \tag{3.2}$$

where $r_0 = 0$ and r_1 is the first minima of the RDF.

Radial distribution functions and coordination numbers were calculated from the geometries optimized with PM7. The atoms were sorted after distance to cations, atomic number and molecule type to obtain a mapping of the solvent structure. The outer limit of the first solvation shell was mapped out by using matlabs *findpeaks()* function and was used as a upper limit when integrating the coordination number of the cation for each atom type.

3.1.5 Ion pair coordination structure

The fraction of ion pairs in SSIP, CIP and AGG structures was calculated from the optimized geometries by defining the conditions for each structure type for the different anions. In Tf the CIP was considered to apply when an anion oxygen was coordinated to a cation, *i.e.* when it had a cation in its first solvation shell, defined as closer than the first minima in the anion oxygen RDF. The anions were considered to be in an AGG if two or more of their oxygens coordinated with different cations or if another anion's oxygen is coordinated to the same cation. The anion was considered to be in SSIP if it did not have any cation in the first anion oxygen solvation shell. An analogous approach was applied to the TFSI anions with coordination between the anion oxygen and the cation as the delimiter. For SCN^- the coordinations considered were between the nitrogen and the cation and between the sulfur and the cation. Again the condition for coordination was weather the cation was closer than the limit of the first solvation shell of the anion atom. Aggregates were considered as an anion coordinating to two different cations and CIP as an anion coordination to one cation.

3.2 Experimental

3.2.1 Preparation of electrolyte

The electrolytes were prepared in the concentrations presented in table 3.1. The concentrations were adjusted based on their solubility in water. The salts that were not already stored in a water free environment were dried in a vacuum oven at 200°C for 24 hours. Salts that were in hydride form underwent a gravimetric analysis in order to determine their water content.

The electrolyte was obtained by carefully weighing salt and water in a vessel. In case of poor solubility the electrolyte was heated to 60°C on a heating plate until the salt was dissolved.

3.2.2 Dielectric spectroscopy

The dielectric measurements were made on a coin cell setup in which the electrolyte was placed in a teflon O-ring between the two sides of the stainless steel case. The instrument used was a Novocontrol dielectric broadband spectrometer. In the dielectric measurement the a.c. voltage was set to 10 mV and both the frequency and temperature were varied. The temperature was set to 9 different values between 273 and 353 K, at each temperature the frequency was varied from 0.13 to 10^6 Hz. In between measurements the o-ring was rinsed with isopropanol and acetone and then dried at 70 °C for 1 hour.

3.2.3 Linear sweep voltammetry

A three electrode T-cell was used for the linear sweep voltammetry measurements. Stainless steel was used as both the working and counter electrode and a silver wire was used as pseudo-reference electrode. Glass fibre was used as a separator. The scan rate was set to 1 mV/s. After each measurement the electrodes were polished to remove residues and the disassembled parts were placed in isopropanol and acetone and cleaned thoroughly using ultrasonic waves for 15 minutes each.

3.2.4 Infrared spectroscopy

The IR spectra were obtained in a Bruker IFS 66v/S Fourier transform infrared spectrometer. A baseline was measured before each spectrum with a clean diamond crystal after pumping vacuum in the sample chamber for 20 minutes. The spectrum was measured by placing a small drop of electrolyte on the crystal of the instrument and again placing the chamber under vacuum for 20 minutes before performing 10 scans over the wavenumbers 520-4000 cm $^{-1}$ with a resolution of 2 cm $^{-1}$.

3.2.5 Raman spectroscopy

The Raman spectra were obtained using a Bruker multiRAM Fourier transform-Raman equipment. The measurements were performed by placing a vessel with the sample in front of the light source, a 1064 nm laser. The sample was aligned in order to provide maximum intensity and make sure that the laser only impinged in the sample. Each measurement was carried out for one hour with 2-3000 scans and a resolution of 4 cm $^{-1}$.

4

Results and Discussion

In this chapter, results obtained from PM7 calculations will be analyzed and discussed followed by analysis and comparison of the results from Raman and LSV measurements, further the conductivity of the electrolytes is presented and the electrolytes are compared on the basis of their qualities as aqueous electrolytes.

4.1 Solvent structure calculations

For all systems under investigation, computational studies have been conducted in order to examine the solvent structure and explain macroscopic properties of the compounds. The radial distribution functions with respect to the cations for the systems are presented in figure 4.1 and the respective peak positions and coordination numbers are presented in table 4.1. Observing the RDFs of systems with TFSI as anion, illustrated on the left side of figure 4.1 one finds large differences in solvent structure depending on which cation is present in the system, in comparison to the differences in structure with change in concentration. All three cations show preference for different atomic spices in the first solvation shell, which is also reflected in the coordination numbers of these systems in table 4.1. We can see that in LiTFSI the lithium cations prefer to surround themselves with oxygen and fluorine from the anion while the sodium cation has a clear preference for correlating to the nitrogen atom of the anions. Magnesium instead correlates with the oxygen of both water molecules and anions. The total coordination numbers are slightly higher in the NaTFSI electrolytes than the LiTFSI and the MgTFSI has a substantially larger coordination number than the two others.

The RDFs for systems with Tf as anion, on the right side of figure 4.1, exhibit less differences with change in cation. The lithium cation in this case also prefers oxygen and fluorine from the anion while for sodium and magnesium the oxygen atoms are preferred before fluorine. Comparing RDFs from the same cation with different anions there are similarities. For the lithium cation the RDFs are very similar for LiTFSI and LiTf, only differing by the additional nitrogen in the LiTFSI electrolyte. Comparing the sodium systems there is a large difference in the shape and peak position of the RDF due to the large nitrogen contribution close to the cation but the remaining parts are similar in composition and placement. In MgTFSI and MgTf there is little difference in the appearence of the RDFs both between concentrations within the same chemistry and between systems with different anions.

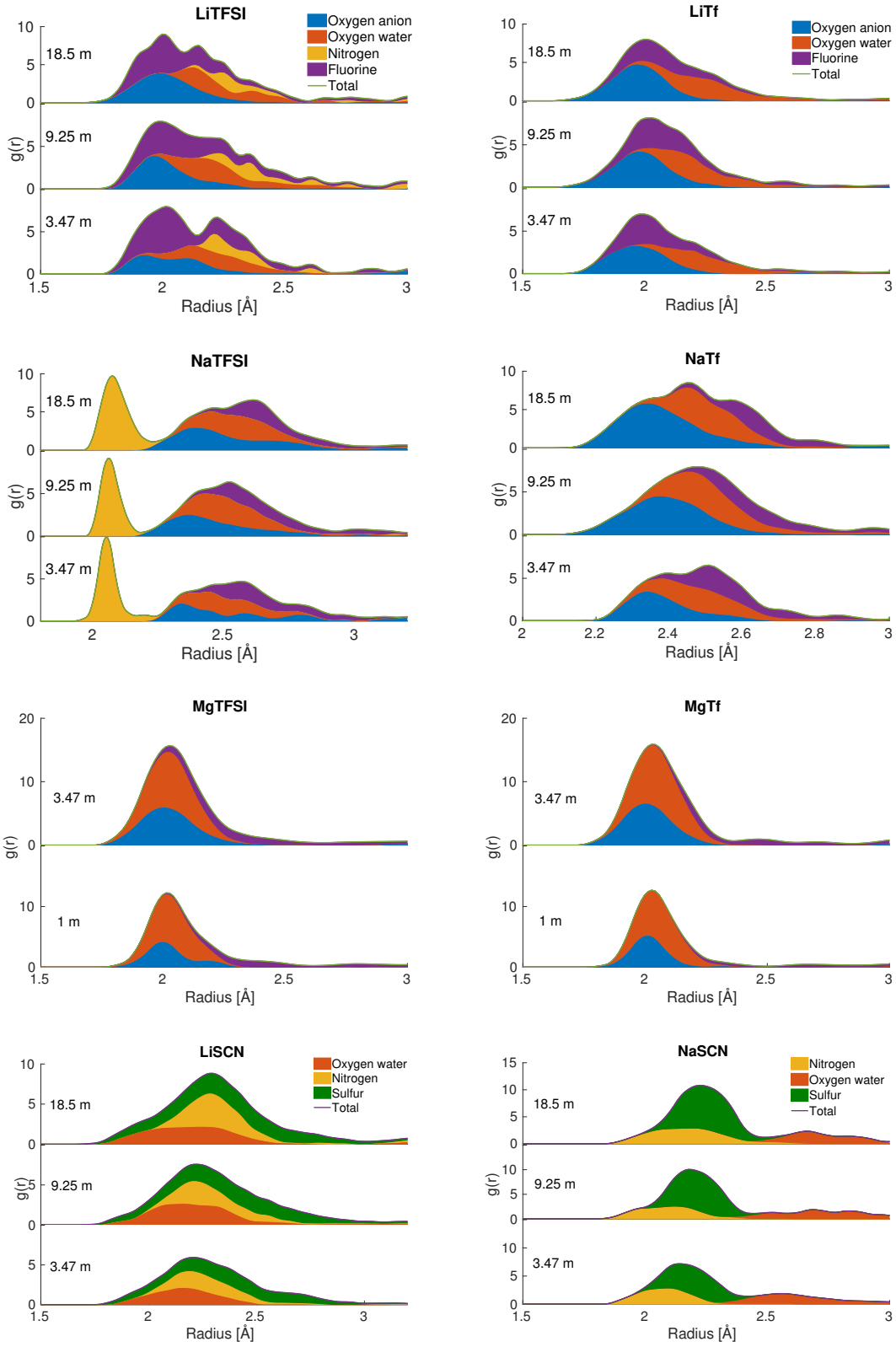

Figure 4.1: Radial distribution functions in relation to cation atoms calculated from solvent structures optimized with PM7.

Table 4.1: Computed partial coordination numbers by atom type for geometries obtained with PM7.

Salt	**C [m]**	$\mathbf{n_{OA}}$	$\mathbf{n_{OW}}$	$\mathbf{n_F}$	$\mathbf{n_N}$	$\mathbf{n_{ONF}}$	$\mathbf{r}_{peak}$
LiTFSI	**3.47**	0.94 (19%)	2.14 (43%)	1.74 (35%)	0.20 (4%)	5.02	2.01
	9.25	1.50 (10%)	1.22 (25%)	2.04 (42%)	0.12 (2%)	4.88	1.98
	18.5	1.94 (37%)	0.56 (11%)	2.56 (49%)	0.16 (3%)	5.22	2.00
NaTFSI	**3.47**	0.84 (17%)	2.72 (54%)	1.12 (22%)	0.4 (8%)	5.08	2.05
	9.25	1.38 (27%)	2.06 (41%)	1.20 (24%)	0.44 (9%)	5.08	2.06
	18.5	2.06 (37%)	1.42 (25%)	1.42 (25%)	0.74 (13%)	5.64	2.07
MgTFSI	**1**	0.48 (8%)	5.24 (85%)	0.46 (7%)	0	6.18	2.01
	3.47	1.64 (26%)	3.66 (58%)	1.00 (16%)	0	6.30	2.03
LiTf	**3.47**	1.02 (24%)	2.08 (50%)	1.10 (26%)	-	4.20	1.98
	9.25	1.48 (35%)	1.41 (33%)	1.33 (32%)	-	4.22	2.03
	18.5	2.16 (46%)	1.19 (25%)	1.38 (29%)	-	4.73	1.98
NaTf	**3.47**	0.82 (18%)	2.89 (65%)	0.72 (16%)	-	4.44	2.40
	9.25	1.85 (39%)	2.25 (47%)	0.65 (14%)	-	4.74	2.48
	18.5	2.60 (55%)	1.42 (30%)	0.72 (15%)	-	4.73	2.45
MgTf	**1**	0.50 (8%)	5.38 (91%)	0.02 (0.3%)	-	5.90	2.03
	3.47	1.51 (23%)	4.69 (72%)	0.27 (4%)	-	6.47	2.03
		$\mathbf{n_S}$	$\mathbf{n_{OW}}$	$\mathbf{n_F}$	$\mathbf{n_N}$	$\mathbf{n_{SOF}}$	$\mathbf{r}_{peak}$
LiSCN	**3.47**	0.54 (15%)	2.70 (73%)	-	0.44 (12%)	3.72	2.21
	9.25	1.06 (27%)	1.90 (48%)	-	0.88 (22%)	4.00	2.22
	18.5	1.34 (33%)	0.70 (17%)	-	0.84 (20%)	4.12	2.30
NaSCN	**3.47**	0.72 (20%)	2.36 (65%)	-	0.40 (11%)	3.64	2.15
	9.25	1.38 (41%)	1.30 (38%)	-	0.48 (14%)	3.4	2.18
	18.5	1.80 (44%)	0.96 (24%)	-	0.78 (19%)	4.06	2.22

In the total coordination numbers from table 4.1 we notice the same trend in the Tf systems as in the TFSI systems with slightly higher coordination numbers for nitrogen than for lithium while magnesium has the largest coordination number. In order to compare the solvation structure between concentrations we turn to the coordination numbers in table 4.1. In general, as expected, we see a decrease of the number of oxygen atoms from water and an increase in atoms belonging to the anions. Looking at how the coordination numbers of specific atomic species change with concentration in the different systems one can see that for oxygen belonging to the anions all systems with TFSI and Tf experience a substantial shift with concentration causing a stronger interaction between anion oxygen and cation at higher concentrations. For the fluorine on the other hand there is only a strong concentration dependence in system LiTFSI, MgTFSI and MgTf where the coordination number for fluorine increase with concentration while in the remaining systems n_F is fairly constant. For the two systems with SCN^- as anion we see the same pattern of decreasing water content and increasing anion content in the solvation shell.

Further the summed up coordination numbers of the different cations in table 4.1 can be compared to coordination numbers of alkali metal ions in water from literature, where the Li^+ cation is said to have a coordination number around 4 and the Na^+ around 5 based on recent experiments[36]. This correspond well considering n_{ONF} for Li^+ is between 4.2 and 5.2 and n_{ONF} of Na^+ lies between 4.4 and 5.6. The n_{SOF} from SCN^- systems are somewhat lower. Mg^{2+} has been found to have a coordination number between 6 and 7 when solvated with TFSI in ethers [37], which fits well with the results shown in table 4.1.

In table 4.1 the peak position of the first solvation shell is presented for each system. Comparing the solvation shell radius of the different compounds shows a constant position of the solvation shell in compounds with TFSI as anion at around 2 Å. For compounds with SCN as anions the r_{peak} is slightly larger at 2.15-2.3 Å. The largest r_{peak} is found in NaTf where the peak experiences a bigger shift to values around 2.4 Å.

The fractions of anions situated in a SSIP, CIP or in AGG was calculated from the optimized geometries, the results are presented in table 4.2. By comparing the fraction of SSIP at different concentrations one can see a clear trend of a decreased fraction SSIP with increased salt concentration for all salts. The opposite trend can be found in the fraction of AGG for all Tf and TFSI salts.

Table 4.2: Fractions of anions and cations in SSIP, CIP and AGG structures calculated from geometries optimized with PM7.

Salt	C [m]	SSIP	CIP	AGG
	3.47	43.3 %	5.0 %	51.7 %
LiTFSI	**9.25**	43.0 %	0.0 %	57.0 %
	18.5	37.4 %	0.0 %	62.6 %
NaTFSI	**3.47**	47.0 %	1.5 %	51.5 %
	9.25	45.2 %	0.0 %	54.8 %
	3.47	31.6 %	45.6 %	22.8 %
LiTf	**9.25**	26.4 %	33.7 %	40.5 %
	18.5	24.2 %	13.6 %	62.1 %
NaTf	**3.47**	51.6 %	29.7 %	18.8 %
	9.25	31.4 %	27.1 %	41.5 %
	3.47	28.0 %	56.0 %	16.0 %
LiSCN	**9.25**	2.0 %	40.0 %	58.0 %
	18.5	6.0 %	46.0 %	48.0 %
	3.47	34.0 %	50.0 %	16.0 %
NaSCN	**9.25**	4.0 %	54.0 %	40.0 %
	18.5	0.0 %	36.0 %	64.0 %

4.2 Molecular orbital analysis

Molecular orbital analysis was performed both at PM7//PM7 and M06-2X/6-311+G* //PM7 level where the systems optimized with PM7 underwent a population analysis with the M06-2X/6-311+G* method and basis set. The onsets of HOMO and LUMO bands and the width of the HOMO-LUMO gap from PM7//PM7 calculations are presented in table 4.3 and the full DOS are plotted in figures A.1 -A.4. For most systems with Na^+ and Li^+ as cations and TFSI and Tf as anions an increase in HOMO-LUMO gap with increased concentration can be noticed. The exceptions are in the compounds with SCN^- as anions where no clear trend can be recognized. Also in compounds with Mg^{2+} as cation we see a decrease in gap with increased concentration.

Table 4.3: Computed onsets for occupied and unoccupied states in density of states obtained from optimized geometries with PM7.

Salt	C [m]	HOMO-onset [eV]	LUMO-onset [eV]	Gap [eV]
LiTFSI	**3.47**	-9.63	-3.66	5.97
	9.25	-9.75	-3.52	6.23
	18.5	-7.65	-5.02	2.63
NaTFSI	**3.47**	-9.58	-3.74	5.84
	9.25	-9.52	-3.60	5.92
	18.5	-10.56	-2.87	7.69
MgTFSI	**1**	-9.26	-3.85	5.41
	3.47	-9.03	-4.32	4.71
LiTf	**3.47**	-9.82	-2.64	7.18
	9.25	-9.93	-2.56	7.37
	18.5	-10.00	-2.31	7.69
NaTf	**3.47**	-9.96	-2.66	7.30
	9.25	-10.14	-2.53	7.61
	18.5	-10.15	-2.41	7.74
MgTf	**1**	-9.74	-4.08	6.14
	3.47	-9.72	-3.60	5.64
LiSCN	**3.47**	-7.25	-1.30	5.95
	9.25	-7.55	-1.35	6.2
	18.5	-7.25	-1.00	6.25
NaSCN	**3.47**	-7.60	-2.55	5.05
	9.25	-7.30	-2.20	5.10
	18.5	-7.6	-3.05	4.55

One interesting result can be noticed for LiTFSI where the largest concentration deviates substantially from the trend of the other two concentrations and the expected behaviour of an increased gap. To further investigate this behaviour, the same analysis was done on DFT level and the resulting DOS is illustrated in figure 4.2. Here, the HOMO/LUMO gap shows a different trend than found in the

PM7 results. The diluted electrolyte now has a HOMO onset around -7 eV and a LUMO onset at -3 eV, giving a gap of 4 eV while the highly concentrated electrolyte has a HOMO shifted to -9.5 eV and a LUMO shifted to -2, giving instead, a widened HOMO/LUMO gap in the highly concentrated electrolyte. This result is more in line with the expected trend considering a linear relationship between the HOMO/LUMO gap and the ESW. The values of the HOMO and LUMO levels calculated from DFT and PM7 orbital information are in close proximity of each other, however showing different trends. This implies that PM7 could be used for rough estimations of the DOS, but can not be relied on in all cases.

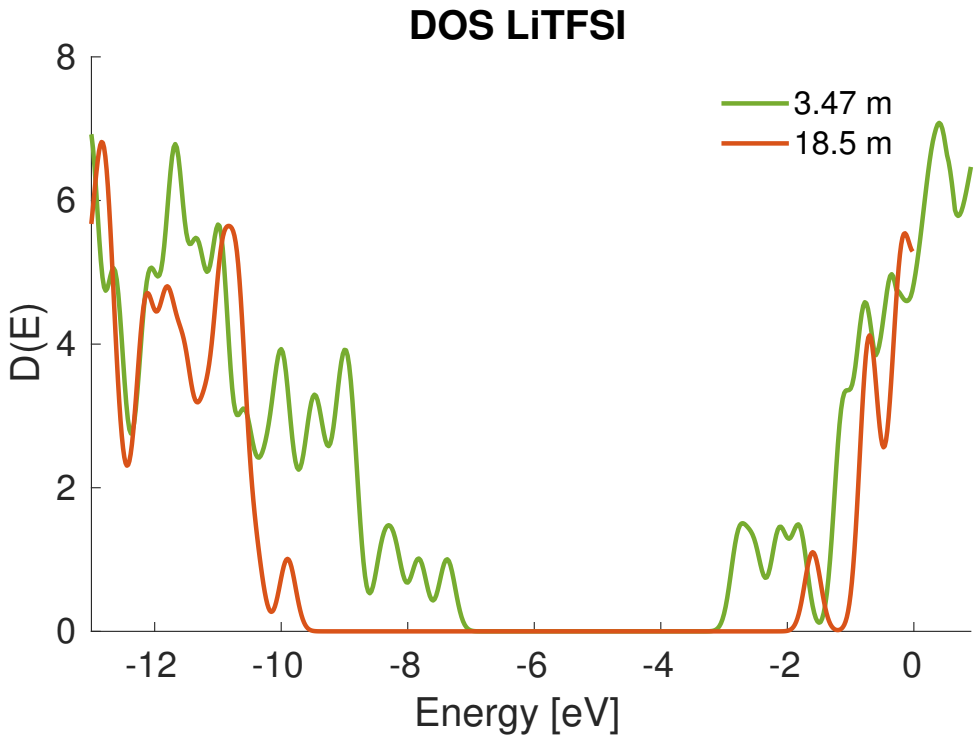

Figure 4.2: Density of states for LiTFSI in different concentrations calculated with M06-2X/6-311+G*//PM7.

4.3 Ionic conductivity

Dielectric spectroscopy was performed on all electrolytes and the conductivity values at 239, 323 and 353 K are presented in table 4.4, the full temperature dependence is shown in figure A.5. The conductivity in the different chemistries seem to diminish with higher salt concentration which can be attributed to the increased viscosity causing lower diffusion coefficients in the electrolytes. The highest conductivities are seen in systems with SCN^-, which is consistent with SCN^- being a small molecule and therefore diffusing easier through the electrolyte. A likewise conclusion can be made when comparing the TFSI and Tf compounds, in general the smaller Tf anion seems to give better conductivity in the electrolyte than the larger TFSI.

Another observation one can make is that the electrolytes with TFSI anions has

Table 4.4: Conductivity and electrochemical stability window (ESW) of the electrolytes at room temperature.

Salt	C [m]	σ [mS/cm]			ESW [V]
		293 K	323 K	353 K	
LiTFSI	**3.47**	58.2	99.0	157.8	2.55
	9.25	61.7	119.0	183.1	2.75
	18.5	16.5	37.3	69.8	3.07
NaTFSI	**3.47**	159.4	296.7	462.9	2.5
	9.25	28.7	85.9	138.4	2.7
	18.5	12.5	28.9	49.5	-
MgTFSI	**1**	63.5	131.1	213.5	2.6
	3.47	22.4	47.6	84.0	2.4
	5	3.0	10.2	43.9	-
LiTf	**3.47**	102.1	171.0	220.1	2.6
	9.25	71.8	130.1	208.7	2.9
	18.5	15.3	33.4	58.1	3.25
NaTf	**3.47**	99.8	183.9	272.6	2.1
	9.25	27.4	134.7	220.8	2.2
	18.5	13.1	32.4	57.1	-
MgTf	**1**	100.9	181.9	246.1	2.05
	3.47	8.1	147.1	252.7	2.4
LiSCN	**3.47**	232.0	374.1	520.4	1.55
	9.25	246.4	399.0	563.0	1.55
	18.5	131.2	236.7	360.5	1.3
NaSCN	**3.47**	282.8	463.1	649.0	1.65
	9.25	125.0	177.9	207.9	1.6
	18.5	60.8	72.4	79.8	1.85

a higher conductivity with Na^+ cations than with the other two cations. This behaviour could be traced to the difference in appearance of the $g(r)$ of the NaTFSI electrolytes compared to LiTFSI and MgTFSI implying a difference in orientation of the anion in relation to the cation, possibly contributing to a larger conduction pathway in the electrolyte.

4.4 Electrochemical stability window

All liquid electrolytes underwent linear sweep voltammetry measurements with stainless steel/stainless steel electrodes and a Ag/Ag^+ pseudo-reference electrode. The voltage gap between the redox onsets was considered as the ESW and these numbers are presented in table 4.4 and in figure 4.3 for a grafical overview. From these values we can see that the LiTFSI, NaTFSI, LiTf, NaTf and MgTf electrolytes all experience ESWs well above the 1.23 V of water and follow the expected trend for a WiSE with expanded ESW at increased salt concentrations. The ESWs of LiTFSI and NaTf are in close proximity of previous results where the ESW of LiTFSI at 21

m was measured to 3.0 V[6] and NaTf at 9.26 m to 2.14 V with inert stainless steel working electrodes and a Ag/AgCl reference electrode[7]. The chemistries which do not seem to follow this trend very well is LiSCN and NaSCN which exhibit the narrowest ESWs and also lack any trend relating ESW width and salt concentration. This can be connected to the lack of pattern shown in the calculated DOS gap of LiSCN and NaSCN presented in table 4.3.

The widest ESW is measured in LiTf at 18.5 m where the width is 3.25 V which is an increase of almost 0.2 V from earlier studied LiTFSI salt. Also the NaTFSI electrolyte at 9.25 m show a widened ESW compared to published sodium WiSEs using NaTF, here the increase in stability window is 0.5 V. One possible explanation why LiTFSI and LiTf show such a wide expansion of the ESW with concentration could be found by analyzing the RDFs of these systems as well as the coordination numbers. Both these systems show a larger tendency for the Li^+ cation to coordinate to the fluorine on the anion compared to the other TFSI and Tf systems. This would suggest that LiF formation is more pronounced than NaF and MgF_2 formation which would lead to a more dense SEI layer and a wider ESW for LiTFSI and LiTf.

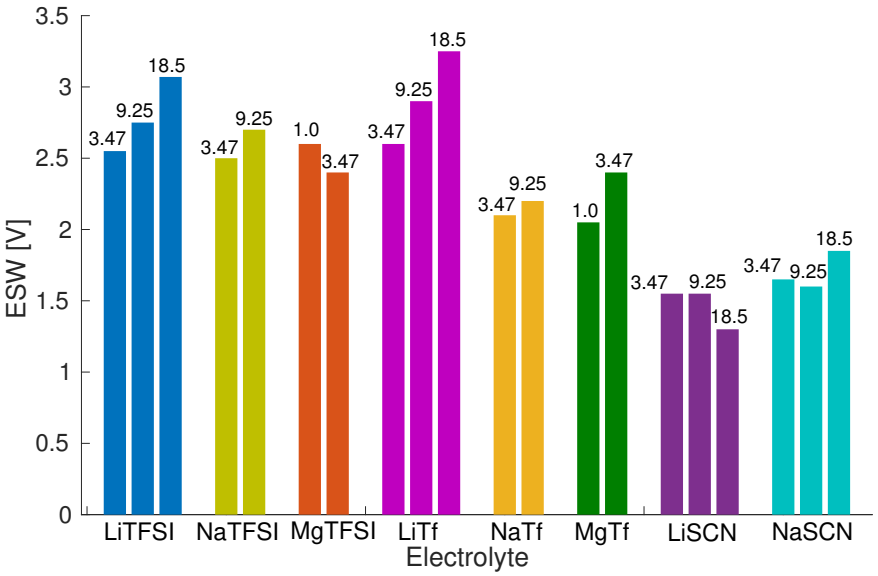

Figure 4.3: Electrochemical stability window by LSV in three-electrode cells with stainless steel working and counter electrodes and a pseudo-reference Ag/Ag^+ electrode and scan rate 1 mV/s. The ESW bars for each electrolyte are marked after salt concentrations in molal.

The LSV measurements of LiTFSI, LiTf, NaTFSI and NaTf are presented in figure 4.4. The LSV results from Mg^+ and SCN^- are presented in figures A.6 and A.7. By studying the behaviour of the LSV curve at potentials close to where the redox reactions occur, we can see some differences in the way the ESW is expanded. The expansion in the ESW of LiTFSI and LiTf are different in the sense that LiTFSI experiences a stabilization in the anodic reaction while LiTf has an increased stability

mainly in the cathodic reaction. Both NaTf and NaTFSI seem to experience a more symmetrical expansion of the ESW implying stabilization against both anodic and cathodic reactions. The insets in figure 4.4 show a plateau in the LSV curves of NaTFSI, LiTf and NaTf before reduction. The plateau current is reduced with concentration but the extent of the plateau is prolonged, stabilizing the electrolyte against full reduction. This behaviour is thought to represent the initial reduction of the electrolyte, forming a SEI which then protects the electrolyte from further reduction[6]. With this argument the prolonged plateau suggest a more rigid SEI formation in the highly concentrated electrolytes, causing a expansion of the ESW.

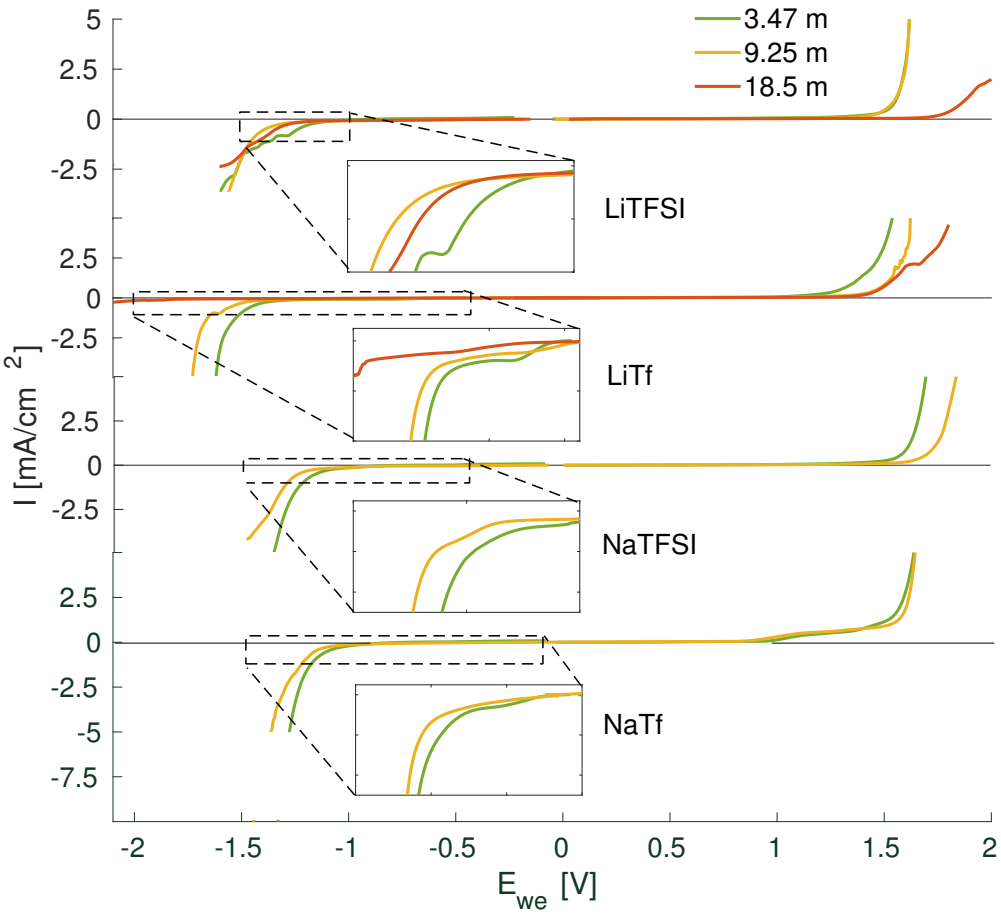

Figure 4.4: LSV of LiTFSI, LiTf, NaTFSI and NaTf respectively, measured in a three-electrode cell with stainless steel working electrodes and a Ag/Ag^+ pseudo-reference electrode at 1 mV/s scan rate. Insets represent enlarged illustrations of the reduction onsets.

4.5 Raman peak shifts

Full Raman spectra of all electrolytes studied can be found in figures A.9 - A.8. The Raman peaks of the S-N-S bending vibration (740 cm^{-1}) of the different TFSI anion systems is shown in figure 4.5. As can be seen, the peak position is shifted towards

higher wavenumbers with increased salt concentration for all systems. This trend, which is confirmed by previous results [6], is especially pronounced for LiTFSI, which shows a shift from 245.23 to 747.97 cm^{-1} while, for MgTFSI the shift in the peak position is not as evident, shifting from 745.18 to 745.62 cm^{-1}. The peak of NaTFSI shifts from 745.43 to 746.24 cm^{-1}. However, it has not been possible to investigate NaTFSI and MgTFSI at higher concentrations due to insolubility and it is probable that these systems at higher concentration would show equal behaviour as that of LiTFSI. This peak is very sensitive to ionic association, so by studying the Raman shift of the S-N-S bending vibration it is possible to determine the structure and positions of the anion and cation. Previous research on pure LiTFSI states that a peak position at 740 cm^{-1} corresponds to uncoordinated TFSI anions, SSIPs, a peak position at 746 cm^{-1} CIPs where the TFSI anions are coordinated to one Li^+ cation while a peak at 748 cm^{-1} corresponds to the formation of AGGs where the anions are coordinated to two cations [38]. From this it can be stated that the concentrations used are sufficiently high to provide CIPs and at high enough concentrations the anions and cations to a larger extent are coordinated as aggregates. Upon formation of aggregates it has been stated that in the LiTFSI system the Li^+ ion surrounds itself with oxygen from the anion which also can be confirmed by the RDF, figure 4.1.

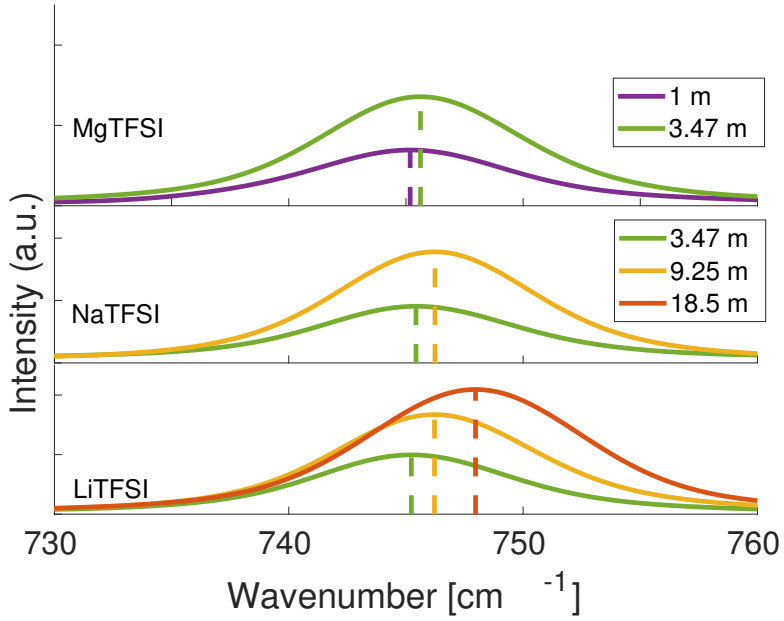

Figure 4.5: Raman spectra of the S-N-S bending vibration of LiTFSI at the concentrations 3.47, 9.25 and 18.5 m, NaTFSI at the concentrations 3.47 and 9.25 m and MgTFSI at the concentrations 1 and 3.47 m.

The Raman spectra of the SO_3 stretching mode (1030 cm^{-1}) of the Tf anion systems is shown in figure 4.6. A shift in this peak to higher wavenumbers with increased concentration has been correlated to aggregation of ionic species [7]. When studying the highest concentration of LiTf, it shows a large shift in the peak position from

1032.9 to 1051.6 indicating that the majority of the ionic species are coordinated as AGGs. This is in good connection with the calculated percentages of ionic species coordinated as SSIPs, CIPs and AGGs as seen in table 4.2, which shows that the amount of AGGs in LiTf increases from 22 to 62 % with concentration. This can also be connected to the widened ESW, see figure 4.3 and table 4.4, since AGGs promotes the formation of LiF which builds up the SEI. Increasing the concentration of MgTf does not lead to a significant shift in the peak position of the SO_3 stretching mode, the peak is shifted from 1032.8 to 1034.1, and hence the formation of aggregates, the anion and cation mainly remain as SSIP. However, this does not seem to be transferable to the ESW considering that the ESW of MgTf is comparable to that of NaTf which show an increased amount of AGGs based on the Raman spectra with a shift from 1034.1 to 1039.8 as well the PM7 calculations. Although, the small shift and yet wide ESW in MgTf could be explained by the amount of anions present in MgTf due to Mg^{2+} being divalent. The high amount of Tf in the system is expected to cause a high fraction of aggregates already at low concentrations, possibly causing less change in solvent structure with concentration.

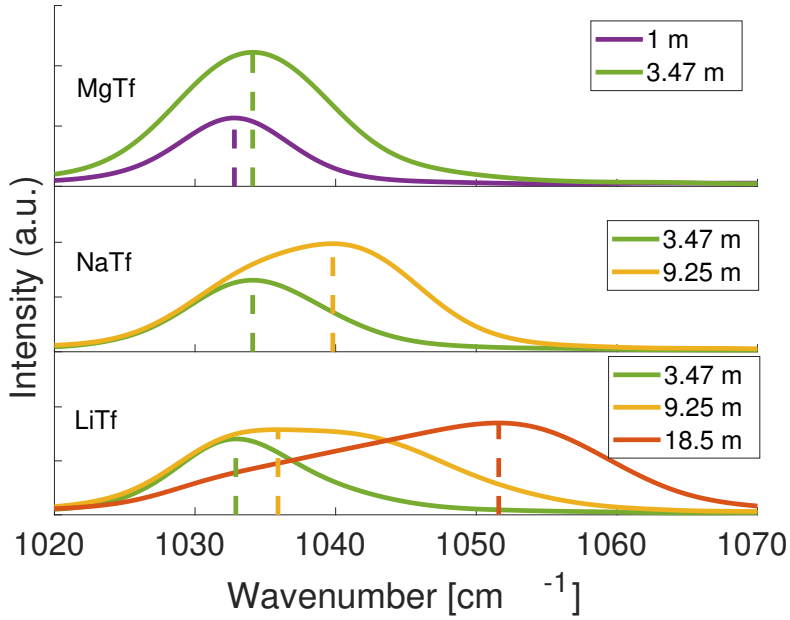

Figure 4.6: Raman spectra of the symmetric SO_3 stretching mode of LiTf at the concentrations 3.47, 9.25 and 18.5 m, NaTf at the concentrations 3.47 and 9.25 m and MgTf at the concentrations 1 and 3.47 m.

Figure 4.7 shows the Raman spectra of the C-S and C-N stretching vibration of the SCN anion systems (750 and 2075 cm^{-1} respectively). As can be seen in figure 4.7 b, the peak position of both NaSCN and LiSCN shifts towards higher frequencies with increased concentration, from 2069.3-2074.4 and 2065-2075.9 cm^{-1} for NaSCN and LiSCN respectively. It should also be noted that the peak of NaSCN become more sharp as the concentration increases. This peak sharpening can be explained by the lack of water in the higher concentrations forcing the SCN^- anion into the

primary solvation shell of the cation [39]. The LiSCN C-S peak also shifts to higher frequencies with increased concentration while NaSCN show a peculiar behaviour where the peak position instead is reduced. It has been stated that shifting of both the C-N and C-S peak depends on whether the cation interacts with the nitrogen or sulfur end of the SCN^- anion[40]. Interaction with nitrogen leads to an increase in both the C-N and C-S peak while interaction with sulfur lowers the C-N peak and increases C-S peak.

An interaction of the cation with nitrogen leads to a shift of the negative charge distribution towards nitrogen and this increases the bond order of C-S. This is contrary to coordination of the cation with sulfur where the shift of the negative charge distribution towards sulfur reduces the bond order of C-S. An increased bond order leads to a larger force constant and hence a shorter interatomic distance. This suggests that an interaction of the cation with nitrogen increases the C-S bond order and the distance between C and S is reduced. This leads to a blue shift in the Raman spectra of the C-S peak [41] as can be seen in figure 4.7 a where the peak of LiSCN is shifted from 752 to 758.7 cm^{-1}. This would suggest that Li^+ coordinates to nitrogen rather than sulfur as the concentration increases as both the C-S and C-N peak positions are shifted to higher wavenumbers. However, it does not explain why the C-S peak position of NaSCN is reduced from 750.6 to 749.7 cm^{-1}

Although the Raman spectra implies that the anion enters into the primary solvation shell of the cation as the concentration increases there is no significant widening of the ESW in either LiSCN or NaSCN. Thus it is likely that a SEI do not form in these systems regardless the proximity of the anion and cation.

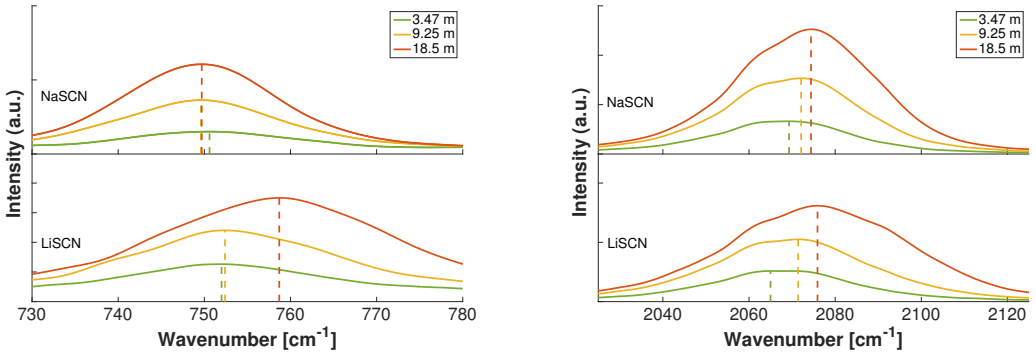

(a) C-S stretching vibration **(b)** C-N stretching vibration

Figure 4.7: Raman spectra of the C-S stretching vibration in the frequency range of 730-780 cm^{-1} and C-N stretching vibration in the frequency range 1025-1125 cm^{-1} of LiSCN and NaSCN at the concentrations 3.47, 9.25, and 18.5 m.

5
Conclusions

This study has aimed in investigating the use of highly concentrated aqueous electrolytes as a complement or replacement to non-aqueous electrolytes used in conventional battery technology today. Both computational and experimental methods have been used to study macroscopic and microscopic properties of these electrolytes. A series of systems (see table 3.1) were chosen based on previous research, cost and abundance and prepared in concentrations ranging from SiWE to WiSE. The aim was to investigate which systems have the tendency to form an SEI and experience an expansion of the ESW at high salt concentrations. This was done by analyzing the solvation structure in terms of RDFs and Raman peak shifts, as well as the electrochemical properties such as electric conductivity, ESW and DOS.

In the majority of the systems studied, an increase in salt concentration resulted in an expanded ESW, the exceptions being MgTFSI, LiSCN and NaSCN where this trend could not be established. Among the studied systems LiTf has the largest ESW. The highest concentration of LiTf and NaTFSI show up to 0.5 V increment in ESW compared to earlier studies in WiSE with the same respective cation. LiTf, NaTf and NaTFSI show a prolonged current plateau before reduction in the LSV curve with increased concentration showing that these electrolytes are stabilized towards reduction. The amount of aggregates in these systems also increased with concentration to more than 40 % and these results both point towards a formation of a SEI. The NaSCN system also show a larger amount of AGGs with increased concentration, however, due to the narrow ESW it is suggested that SCN^- do not participate in the formation of an SEI and that the decomposed products of the electrolyte are incapable of depositing on the electrode surface. It seems as though an electrolyte system containing fluorine is required for a formation of an SEI and an expanded ESW. The electrolytes based on a divalent cation has in this study showed a low conductivity as well as a poor solubility. However, already at low concentrations MgTFSI and MgTf show an expanded ESW resulting in both a more environmentally and economically sustainable electrolyte system.

To build on this work, a continuation could be to build a battery cell with promising candidates with a wide ESW like LiTf, NaTFSI and MgTFSI to test coloumbic efficiency and energy density of the full cells. Further, transmission electron miscroscopy and X-ray diffraction analysis of the cycled electrodes could be used to confirm or reject the hypothesis of SEI formation. One could also expand the computational study to include DOS calculated in DFT for all systems to further establish electronic properties behind the experimental results in NaSCN and LiSCN.

Bibliography

[1] "International energy outlook 2017," tech. rep., USDOE Energy Information Administration (EIA), Washington, DC (United States). Office of Energy Analysis, 2017.

[2] "Goal 13: Take urgent action to combat climate change and its impacts." https://www.un.org/sustainabledevelopment/climate-change-2/. Accessed: 2018-03-21.

[3] "Paris agreement signing ceremony – 22 april 2016." https://www.un.org/sustainabledevelopment/parisagreement22april/. Accessed: 2018-03-21.

[4] M. Dresselhaus and I. Thomas, "Alternative energy technologies," *Nature*, vol. 414, no. 6861, p. 332, 2001.

[5] M. Armand and J.-M. Tarascon, "Building better batteries," *nature*, vol. 451, no. 7179, p. 652, 2008.

[6] L. Suo, O. Borodin, T. Gao, M. Olguin, J. Ho, X. Fan, C. Luo, C. Wang, and K. Xu, ""water-in-salt" electrolyte enables high-voltage aqueous lithium-ion chemistries," *Science*, vol. 350, no. 6263, pp. 938–943, 2015.

[7] L. Suo, O. Borodin, Y. Wang, X. Rong, W. Sun, X. Fan, S. Xu, M. A. Schroeder, A. V. Cresce, F. Wang, *et al.*, ""water-in-salt" electrolyte makes aqueous sodium-ion battery safe, green, and long-lasting," *Advanced Energy Materials*, vol. 7, no. 21, 2017.

[8] J.-K. Park, *Principles and applications of lithium secondary batteries*. John Wiley & Sons, 2012.

[9] L. Zhang, J. Jung, and J. Zhang, *Lead-acid battery technologies: fundamentals, materials, and applications*. CRC Press, 2015.

[10] Y. Wu, *Lithium-ion batteries: Fundamentals and Applications*, vol. 4. CRC Press, 2015.

[11] D. Lide, *CRC Handbook of Chemistry and Physics, 88th Edition*. Taylor & Francis, 2007.

[12] M. Ue, Y. Sasaki, Y. Tanaka, and M. Morita, "Nonaqueous electrolytes with advances in solvents," in *Electrolytes for Lithium and Lithium-Ion Batteries*, pp. 93–165, Springer, 2014.

[13] L. Suo, D. Oh, Y. Lin, Z. Zhuo, O. Borodin, T. Gao, F. Wang, A. Kushima, Z. Wang, H.-C. Kim, *et al.*, "How solid-electrolyte interphase forms in aqueous electrolytes," *Journal of the American Chemical Society*, vol. 139, no. 51, pp. 18670–18680, 2017.

[14] E. Peled and S. Menkin, "Sei: past, present and future," *Journal of The Electrochemical Society*, vol. 164, no. 7, pp. A1703–A1719, 2017.

[15] "Bis(trifluoromethane)sulfonimide lithium salt." https://www.sigmaaldrich.com/catalog/product/aldrich/449504?lang=en&region=SE&gclid=CjwKCAjwi6TYBRAYEiwAOeH7GRjC_VWxNuPL-JfgRstSViZjEvn4W3aCq1VWU7FOpYWl8uaVP4nS1BoCXmoQAvD_BwE. Accessed: 2018-05-26.

[16] O. Borodin, L. Suo, M. Gobet, X. Ren, F. Wang, A. Faraone, J. Peng, M. Olguin, M. Schroeder, M. S. Ding, *et al.*, "Liquid structure with nano-heterogeneity promotes cationic transport in concentrated electrolytes," *ACS nano*, vol. 11, no. 10, pp. 10462–10471, 2017.

[17] J. Ho, M. L. Coote, C. J. Cramer, and D. G. Truhlar, "Theoretical calculation of reduction potentials," *Organic electrochemistry*, vol. 5, 2012.

[18] K. Ramachandran, G. Deepa, and K. Namboori, *Computational chemistry and molecular modeling: principles and applications*. Springer Science & Business Media, 2008.

[19] L. H. Thomas, "The calculation of atomic fields," *Mathematical Proceedings of the Cambridge Philosophical Society*, vol. 23, no. 5, p. 542–548, 1927.

[20] E. Fermi, "Un metodo statistico per la determinazione di alcune priorieta dell'atome," *Rend. Accad. Naz. Lincei*, vol. 6, no. 602-607, p. 32, 1927.

[21] P. Hohenberg and W. Kohn, "Inhomogeneous electron gas," *Physical review*, vol. 136, no. 3B, p. B864, 1964.

[22] Y. Zhao and D. G. Truhlar, "The m06 suite of density functionals for main group thermochemistry, thermochemical kinetics, noncovalent interactions, excited states, and transition elements: two new functionals and systematic testing of four m06-class functionals and 12 other functionals," *Theoretical Chemistry Accounts*, vol. 120, no. 1-3, pp. 215–241, 2008.

[23] R. Dick *et al.*, *Advanced Quantum Mechanics*. Springer, 2012.

[24] B. Van Zeghbroeck, "Principles of semiconductor devices," 2004.

[25] P. Larkin, *Infrared and Raman spectroscopy: principles and spectral interpretation*. Elsevier, 2017.

[26] "The essential principles of infrared absorption and raman scattering," in *Handbook of Fourier Transform Raman and Infrared Spectra of Polymers* (A. Kuptsov and G. Zhizhin, eds.), vol. 45 of *Physical Sciences Data*, Elsevier, 1998.

[27] D. Wolverson, "Chapter 17 - raman spectroscopy," in *Characterization of Semiconductor Heterostructures and Nanostructures (Second Edition)* (C. Lamberti, , and G. Agostini, eds.), pp. 753 – 802, Oxford: Elsevier, second edition ed., 2013.

[28] F. Kremer, A. Huwe, A. Schönhals, and S. Rózanski, *Broadband Dielectric Spectroscopy*. Springer, 2012.

[29] C. Eaborn, "Comprehensive chemical kinetics," 1978.

[30] D. Van Der Spoel, E. Lindahl, B. Hess, G. Groenhof, A. E. Mark, and H. J. Berendsen, "Gromacs: fast, flexible, and free," *Journal of computational chemistry*, vol. 26, no. 16, pp. 1701–1718, 2005.

[31] "Avogadro: an open-source molecular builder and visualization tool. version 1.2.0." http://avogadro.cc/.

[32] M. D. Hanwell, D. E. Curtis, D. C. Lonie, T. Vandermeersch, E. Zurek, and G. R. Hutchison, "Avogadro: an advanced semantic chemical editor, visualization, and analysis platform," *Journal of cheminformatics*, vol. 4, no. 1, p. 17, 2012.

[33] M. J. Frisch, G. W. Trucks, H. B. Schlegel, G. E. Scuseria, M. A. Robb, J. R. Cheeseman, G. Scalmani, V. Barone, G. A. Petersson, H. Nakatsuji, X. Li, M. Caricato, A. V. Marenich, J. Bloino, B. G. Janesko, R. Gomperts, B. Mennucci, H. P. Hratchian, J. V. Ortiz, A. F. Izmaylov, J. L. Sonnenberg, D. Williams-Young, F. Ding, F. Lipparini, F. Egidi, J. Goings, B. Peng, A. Petrone, T. Henderson, D. Ranasinghe, V. G. Zakrzewski, J. Gao, N. Rega, G. Zheng, W. Liang, M. Hada, M. Ehara, K. Toyota, R. Fukuda, J. Hasegawa, M. Ishida, T. Nakajima, Y. Honda, O. Kitao, H. Nakai, T. Vreven, K. Throssell, J. A. Montgomery, Jr., J. E. Peralta, F. Ogliaro, M. J. Bearpark, J. J. Heyd, E. N. Brothers, K. N. Kudin, V. N. Staroverov, T. A. Keith, R. Kobayashi, J. Normand, K. Raghavachari, A. P. Rendell, J. C. Burant, S. S. Iyengar, J. Tomasi, M. Cossi, J. M. Millam, M. Klene, C. Adamo, R. Cammi, J. W. Ochterski, R. L. Martin, K. Morokuma, O. Farkas, J. B. Foresman, and D. J. Fox, "Gaussian~16 Revision A.03," 2016. Gaussian Inc. Wallingford CT.

[34] J. J. Stewart, "Mopac2016." `HTTP://OpenMOPAC.net`, 2016.

[35] "The radial distribution functions: definitions." `http://isaacs.sourceforge.net/phys/rdfs.html`. Accessed: 2018-04-15.

[36] S. Varma and S. B. Rempe, "Coordination numbers of alkali metal ions in aqueous solutions," *Biophysical Chemistry*, vol. 124, no. 3, pp. 192 – 199, 2006.

[37] T. Watkins and D. A. Buttry, "Determination of mg2+ speciation in a tfsi—based ionic liquid with and without chelating ethers using raman spectroscopy," *The Journal of Physical Chemistry B*, vol. 119, no. 23, pp. 7003–7014, 2015.

[38] D. M. Seo, O. Borodin, S.-D. Han, P. D. Boyle, and W. A. Henderson, "Electrolyte solvation and ionic association ii. acetonitrile-lithium salt mixtures: highly dissociated salts," *Journal of The Electrochemical Society*, vol. 159, no. 9, pp. A1489–A1500, 2012.

[39] N. Rohman, A. Wahab, N. N. Dass, and S. Mahiuddin, "Viscosity, electrical conductivity, shear relaxation time and raman spectra of aqueous and methanolic sodium thiocyanate solutions," *Fluid phase equilibria*, vol. 178, no. 1-2, pp. 277–297, 2001.

[40] P. W. Schultz, G. E. Leroi, and A. I. Popov, "Solvation of scn-and secn-anions in hydrogen-bonding solvents," *Journal of the American Chemical Society*, vol. 118, no. 43, pp. 10617–10625, 1996.

[41] P. Schultz, "Ab initio calculations of ionic and hydrogen bonding interactions with the ocn-, scn-and secn-anions," *Molecular Physics*, vol. 88, no. 1, pp. 217–246, 1996.

A

Appendix

A.1 Density of states

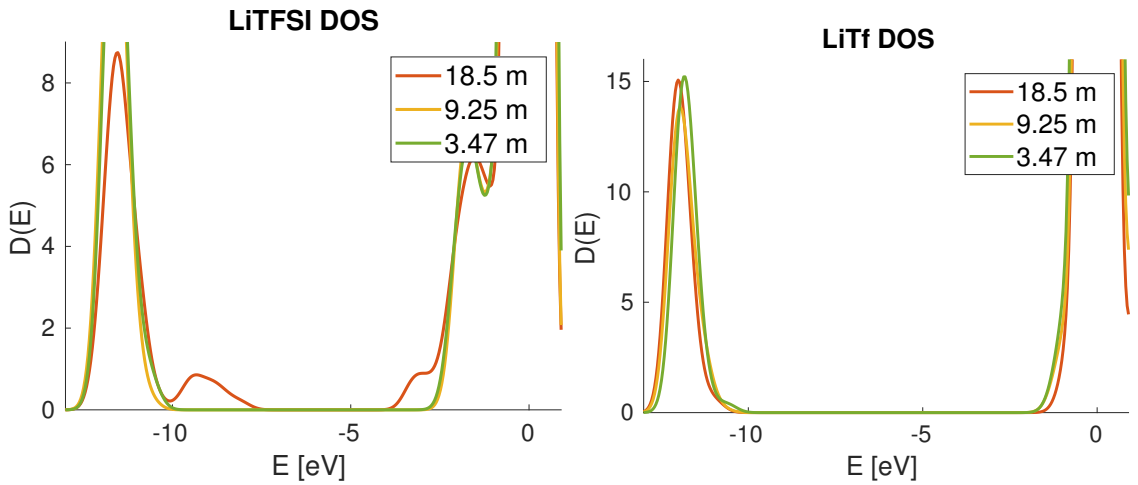

(a) (b)

Figure A.1: Density of states computed with PM7 for aqueous electrolytes with LiTFSI (a) and LiTf (b) salt respectively.

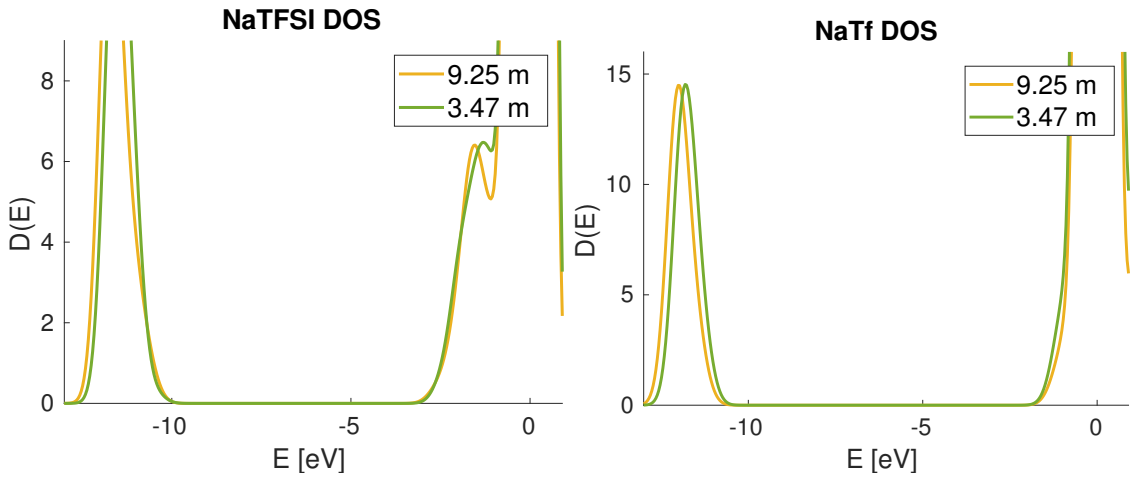

(a) (b)

Figure A.2: Density of states computed with PM7 for aqueous electrolytes with NaTFSI (a) and NaTf (b) salt respectively.

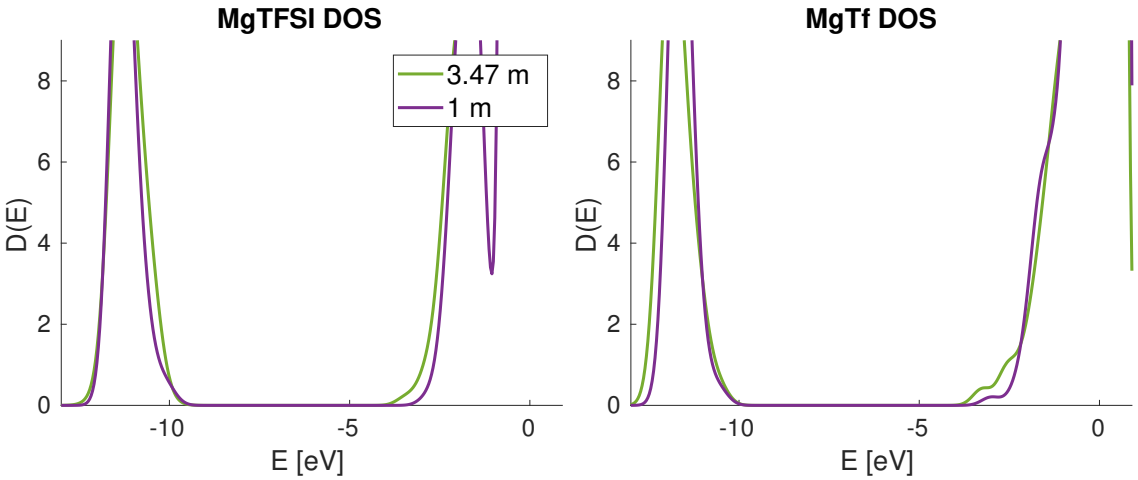

(a) (b)

Figure A.3: Density of states computed with PM7 for aqueous electrolytes with MgTFSI (a) and MgTf (b) salt respectively.

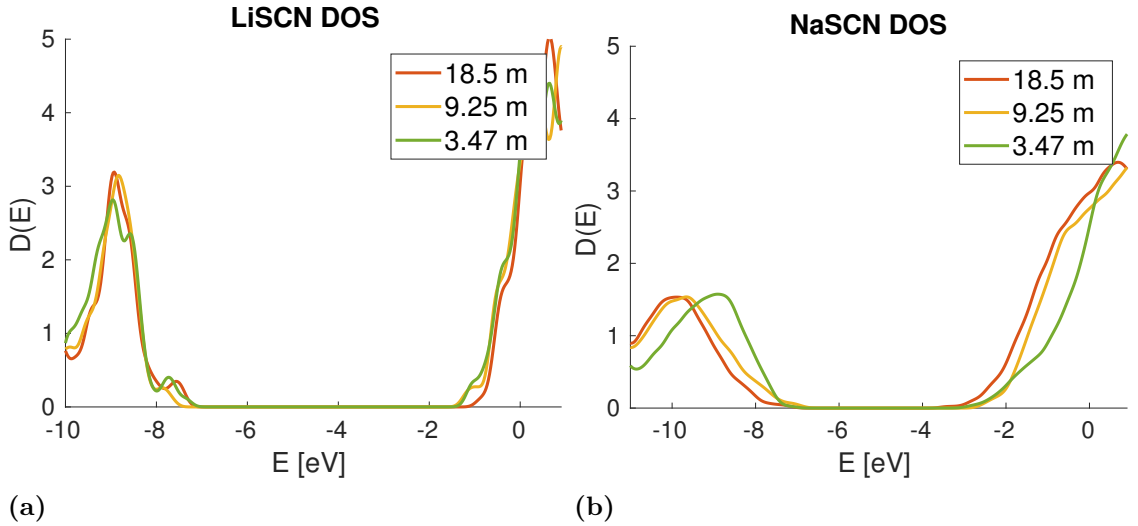

(a) (b)

Figure A.4: Density of states computed with PM7 for aqueous electrolytes with LiSCN (a) and NaSCN (b) salt respectively.

A.2 Ionic conduvtivity

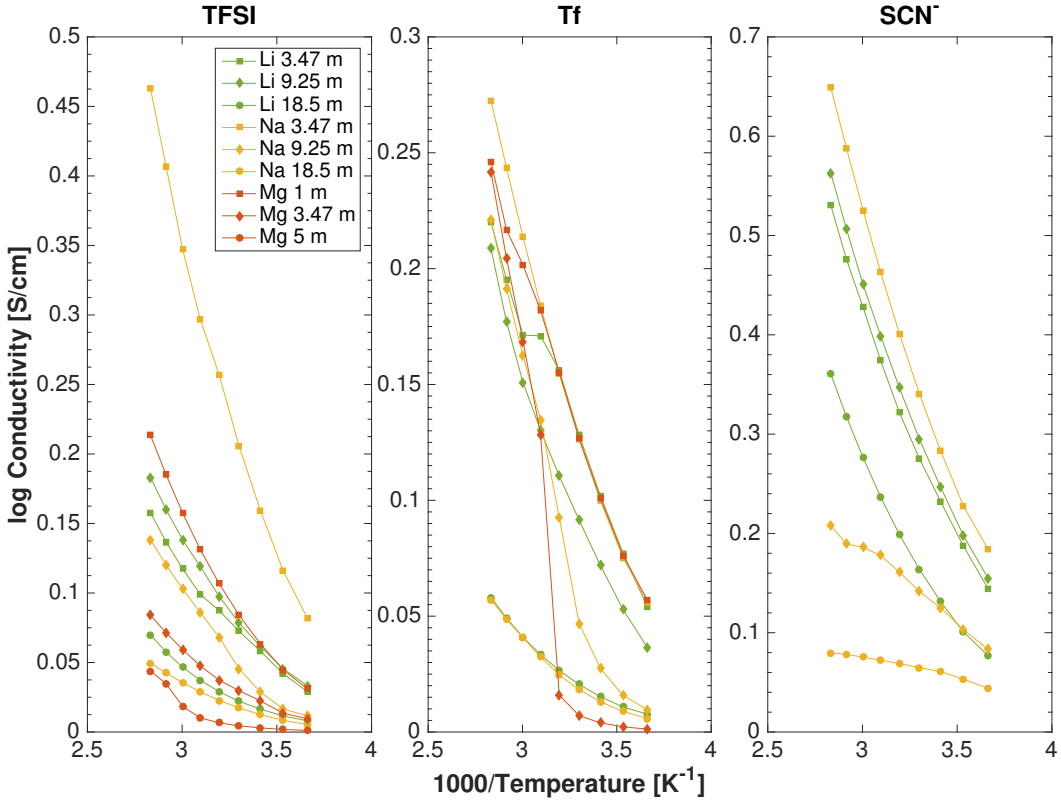

Figure A.5: Conductivity of the different electrolytes as a function of temperature.

A.3 ESW

The magnesium electrolytes show different behaviour with increased salt concentration. In MgTFSI we see a narrowing of the ESW with an increase in concentration while for MgTf we see a widening of the ESW. The LSV for both systems are plotted in figure A.6. The insets show a current plateau in the reduction reaction for both chemistries with the difference that for MgTFSI even tho the plateau current is reduced with increased concentration the plateau is not prolonged, leading to reduction earlier. In the MgTf system the plateau is reduced and prolonged leading to a widened ESW at 3.47 m.

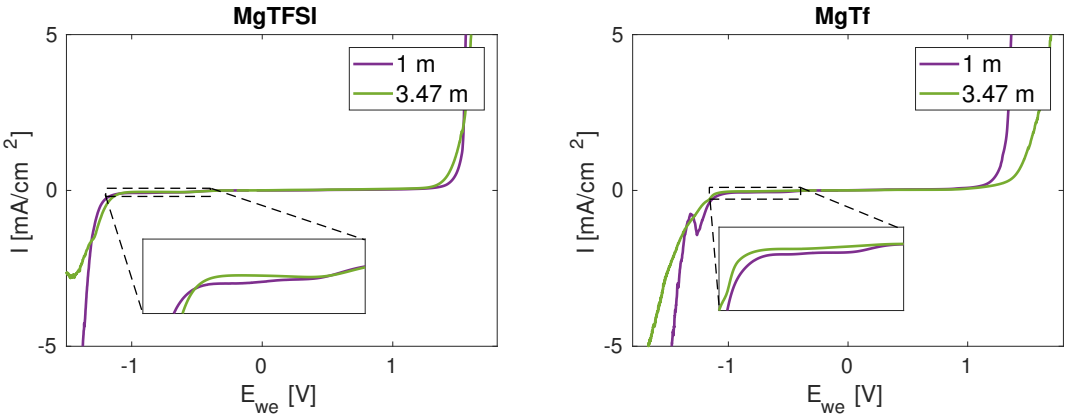

(a) (b)

Figure A.6: LSV for MgTFSI (a) and MgTf (b) measured in a three electrode T-cell with stainless steel counter- and working electrode and a silver wire as pseudo-reference electrode. The insets show enlarged illustrations of the reduction reaction.

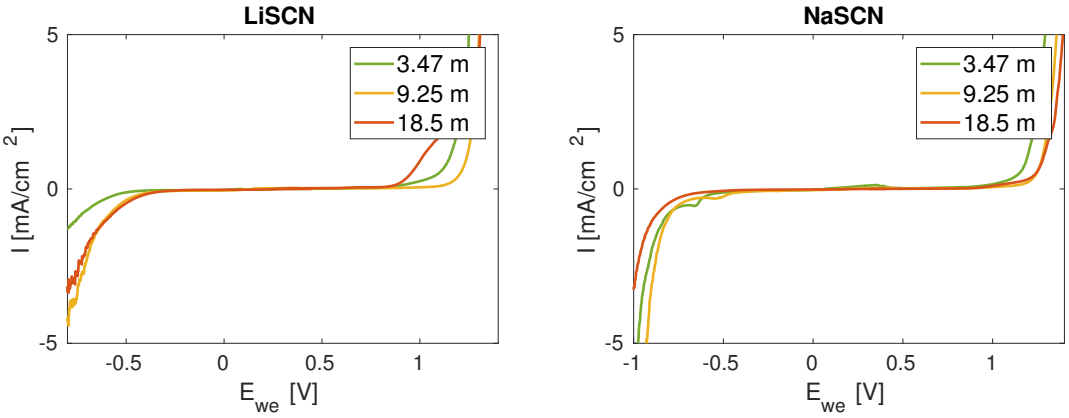

(a) (b)

Figure A.7: LSV for LiSCN (a) and NaSCN (b) measured in a three electrode T-cell with stainless steel counter- and working electrode and a silver wire as pseudo-reference electrode.

A.4 Raman spectra

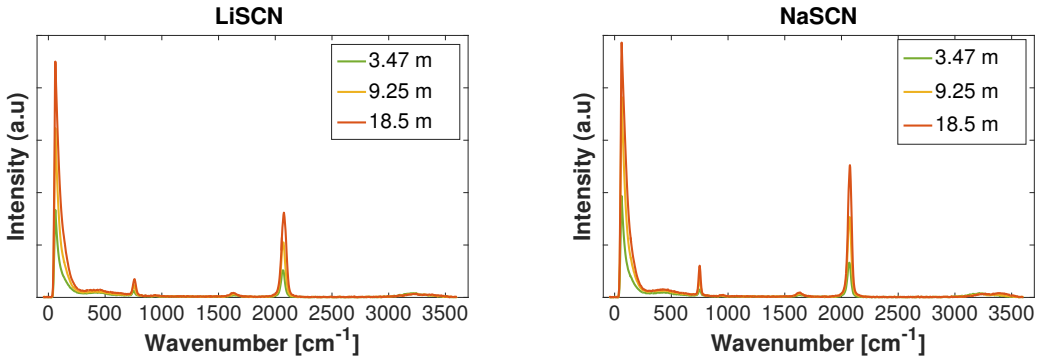

(a) (b)

Figure A.8: Raman spectra of LiSCN (a) and NaSCN (b) at the concentrations 3.47, 9.25 and 18.5 m in the frequency range 0-3700 cm $^{-1}$.

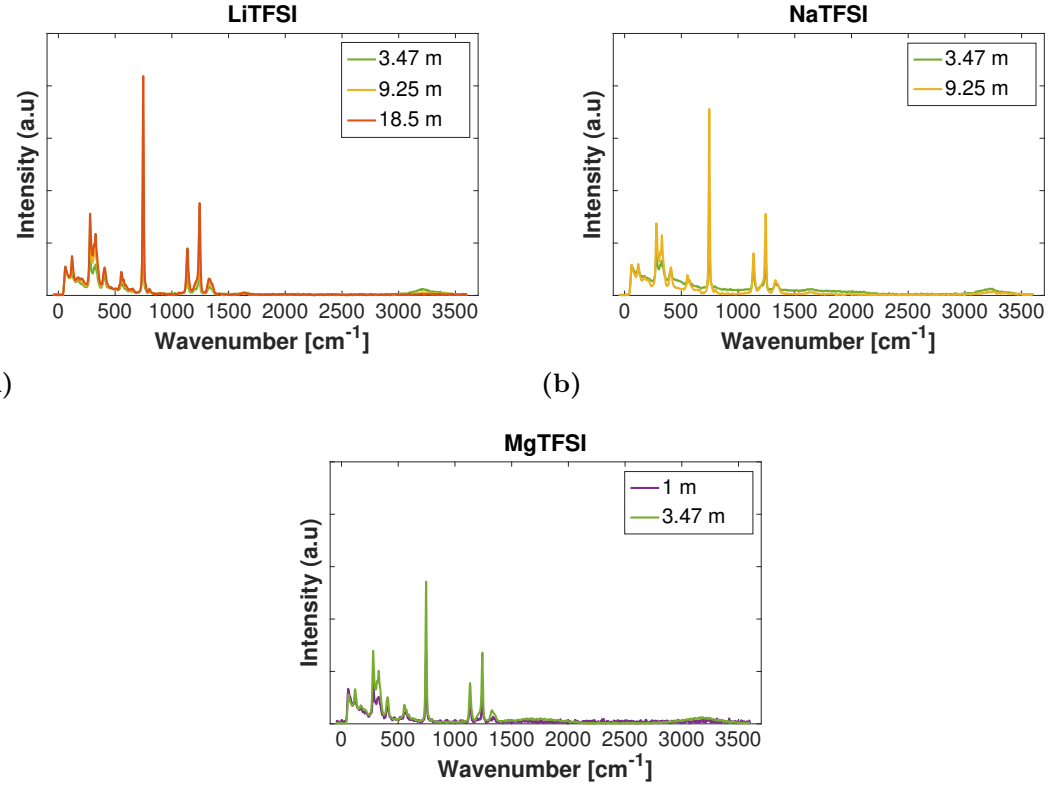

(a) (b)

(c)

Figure A.9: Raman spectra of LiTFSI (a) at the concentrations 3.47, 9.25 and 18.5 m, NaTFSI (b) at the concentrations 3.47 and 9.25 m and MgTFSI at the concentrations 1 and 3.47 m (c). All in the frequency range 0-3700 cm $^{-1}$.

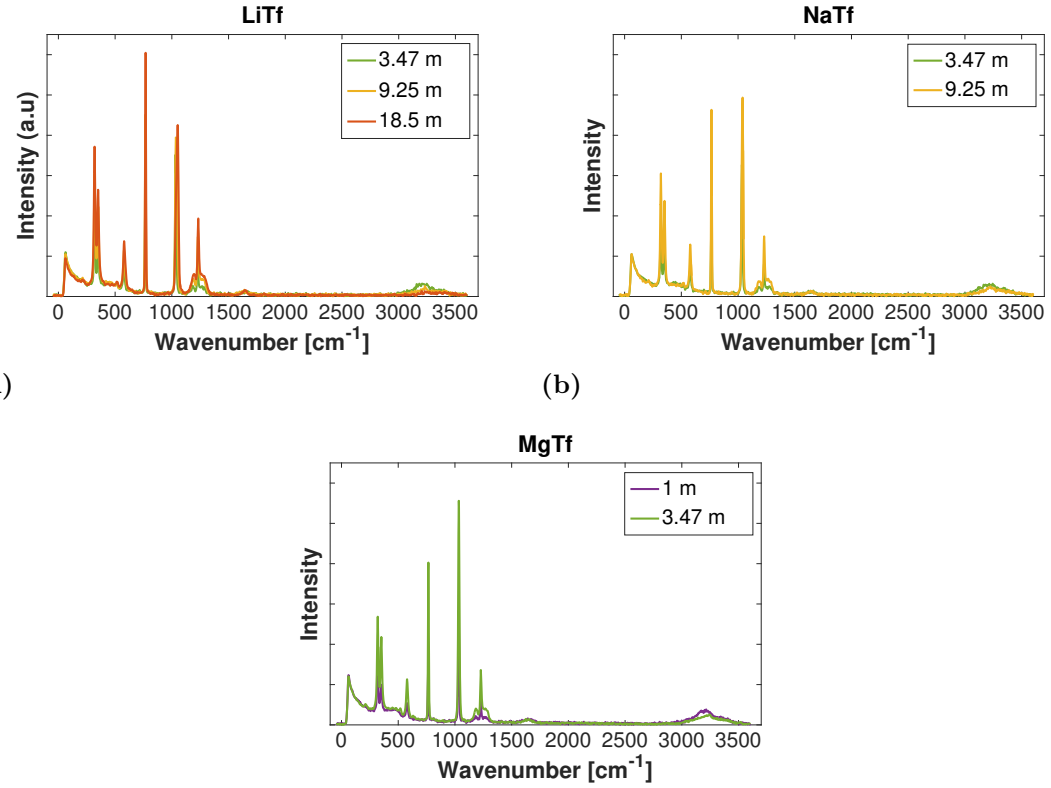

Figure A.10: Raman spectra of LiTf (a) at the concentrations 3.47, 9.25 and 18.5 m, NaTf (b) at the concentrations 3.47 and 9.25 m and MgTf at the concentrations 1 and 3.47 m (c). All in the frequency range 0-3700 cm $^{-1}$.

A.5 IR spectra

The IR spectra of the different electrolyte systems can be seen in figures A.11 to A.13 below. The peak at approximately 3250 cm $^{-1}$ corresponds to the vibrations of the water molecules. It is expected that the intensity of this peak would decrease with an increase in concentration. However, this trend can not be spotted for many of the systems, looking specifically at LiTFSI, LiTf, LiSCN and NaSCN. This indicates that some of the water may have evaporated leading to incorrect measurements why it is difficult to draw any conclusions regarding the molecular structures of the electrolytes based on the IR spectra.

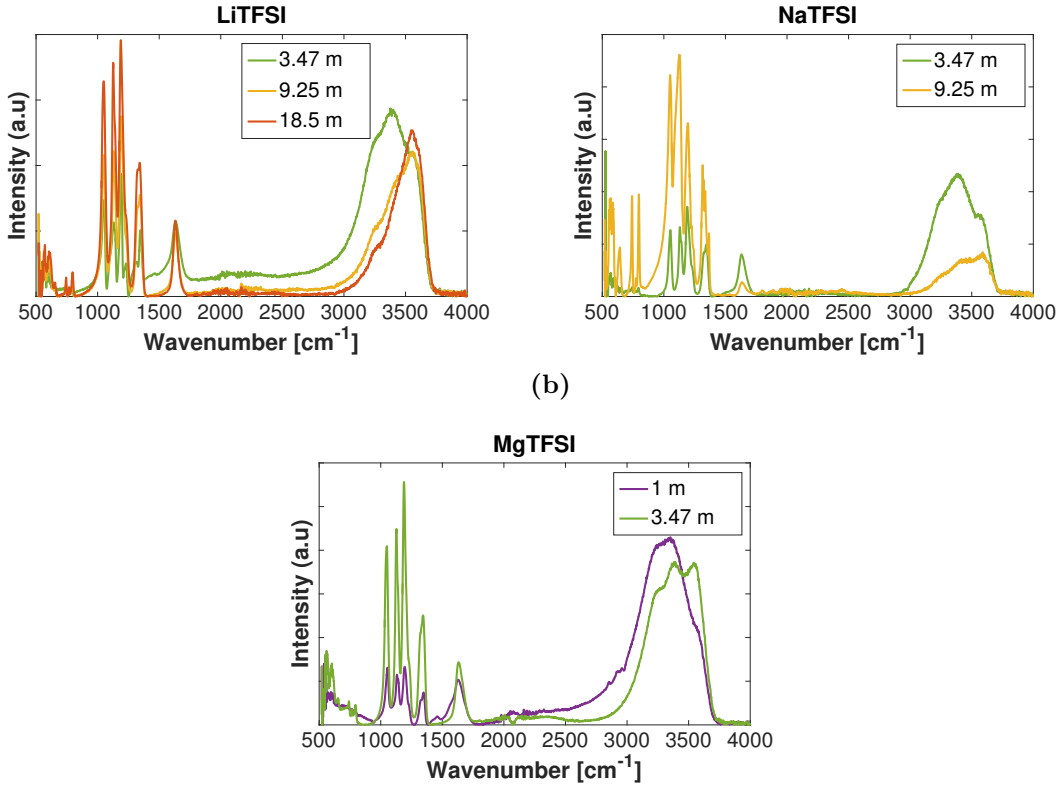

Figure A.11: IR spectra of LiTFSI (a) at the concentrations 3.47, 9.25 and 18.5 m, NaTFSI (b) at the concentrations 3.47 and 9.25 m and MgTFSI at the concentrations 1 and 3.47 m (c). All in the frequency range 500-4000 cm $^{-1}$.

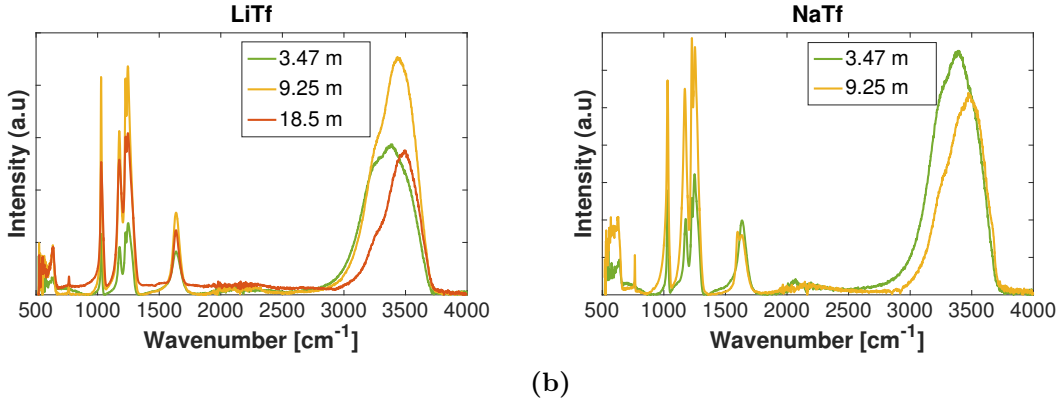

Figure A.12: IR spectra of LiTf (a) at the concentrations 3.47, 9.25 and 18.5 m, NaTf (b) at the concentrations 3.47 and 9.25 m and MgTf at the concentrations 1 and 3.47 m (c). All in the frequency range 500-4000 cm $^{-1}$.

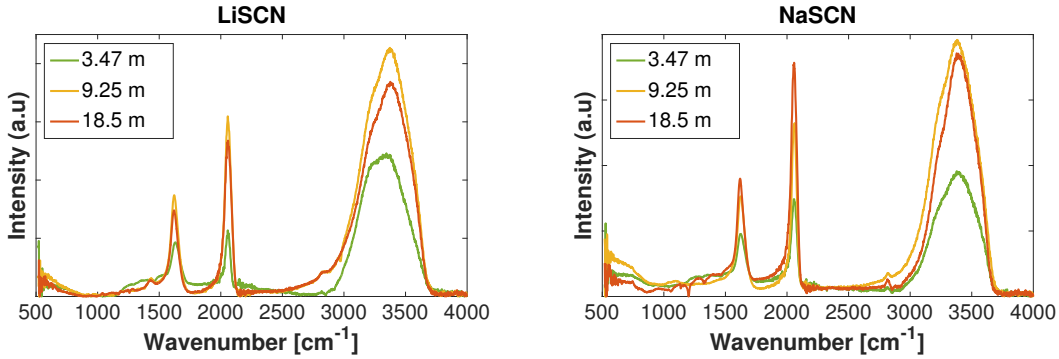

(a) **(b)**

Figure A.13: IR spectra of LiSCN (a) and NaSCN (b) at the concentrations 3.47, 9.25 and 18.5 m in the frequency range 500-4000 cm $^{-1}$.